Ocean acoustic interferometry

DOCTORAL THESIS

12th October 2008

Author: Laura A. Brooks

Supervisor:	Assoc. Prof. Anthony C. Zander [†]
Co-supervisors:	Dr Peter Gerstoft [††]
	Prof. Colin H. Hansen [†]
	Dr Z. Yong Zhang [*]

[†]School of Mechanical Engineering, The University of Adelaide, Australia
[††]Marine Physical Laboratory, Scripps Institution of Oceanography, USA
[*]Defence Science and Technology Organisation, Edinburgh, Australia

Chapter 1

Introduction

The attenuation of sound as it travels through water is significantly less than that of light or radio waves and therefore acoustics is the preferred means of underwater exploration, communication and target acquisition.

Acoustic signals recorded on a hydrophone, or an array of hydrophones, contain information about the environment in which they are measured. The relationship between recorded acoustic signals and the ocean environment has been an important area of research since submarines took an active role in defence in the First World War, and much of the fundamental material has since been documented [1–5]. Theoretical relationships between the environment and acoustic propagation within it can be determined for simple environments, but a realistic ocean environment requires numerical methods to solve for acoustic propagation. Full inversion techniques have traditionally been employed to analyse hydrophone data in attempts to characterise properties of the waveguide environment and to define underlying sediment properties [6]. The main drawbacks of these techniques are that optimisation over multiple variables results in a computationally expensive problem, and uniqueness problems often occur.

The Green's function between two points is the point source solution of the governing acoustic propagation equations (i.e., it is the signal that would be received at one point given a unit impulsive source at the other).

It is fully dependent upon the geometry and environment under consideration, and therefore can be used to determine information about the environment, in this case the ocean waveguide and the underlying sediment, through which acoustic transmission between the two points takes place. Approximation of the acoustic Green's function in the ocean using simple processing techniques is therefore an exciting prospect.

The most straightforward method of determining the Green's function between two points A and B is to excite a source at one of the points, A say, and record the subsequent signal at a receiver located at B. The Green's function is then extracted from the received signal by deconvolution with the source signal.

It has been shown that good estimates of the acoustic Green's function between two points can be determined from cross-correlations of diffuse sound fields [7]. This concept, which eliminates the requirement of having a source at either location, has been successfully applied to problems in ultrasonic noise [8–10], ambient noise in a homogeneous medium [11], seismic noise [12–19], moon-seismic noise [20], and even human skeletal muscle noise [21].

To obtain an accurate representation of the Green's function between two receivers, there is a local requirement that waves propagate on average isotropically near both receivers [13]. This could theoretically be achieved in the ocean by locating the two points between which the Green's function is to be estimated within a volume distribution of sources. Such a configuration is, however, unrealistic in practice.

The ocean noise field is dominated by wave generated noise above a few hundred Hertz [22–24] and shipping noise below about $100\,\text{Hz}$ [22, 23]. Wave generated ambient noise is concentrated near the ocean surface, and although it gives an approximately uniform sheet of sources, the absence of sources lower in the waveguide means that the ocean acoustic modes are not all excited. As a result, time-averaged cross-correlations of ocean surface wave noise will produce accurate inter-hydrophone travel times, but

incorrect amplitudes [15]. Ship sources give low frequency high amplitude signals, which have high coherence over greater distances. The distribution of these sources, also concentrated near the surface, is less uniform than wave generated noise, but cross-correlations over a sufficiently long interval should yield an amplitude shaded Green's function (i.e., a Green's function convolved with amplitude factors) similar to that obtained from ocean wave noise [25, 26].

Biological organisms, such as fish, can give a quasi-volume source distribution, but again, they tend not to span the entire depth of the water column. Travel times have successfully been extracted from cross-correlation of croaker fish dominated noise [27].

Alternate source configurations can be achieved using active sources. For example, a simplification of a volume distribution can be achieved using a vertical column of sources, which can potentially excite all water-borne modes.

There are less than a dozen refereed papers in the literature that address Green's function approximation from acoustic cross-correlations in the ocean. The work in this thesis therefore aims to further the understanding of the Green's function approximation between two points in a shallow water ($<100\,\mathrm{m}$) oceanic waveguide without having a source at either location. The approach of inferring the Green's function between two receivers from signal cross-correlation in the ocean is referred to here as *ocean acoustic interferometry*, due to its relationship to classical and seismic interferometry [28]. This thesis focusses upon ocean acoustic interferometry using two source types: active sources, and opportunistic ship noise. Ship noise has the advantage of no additional source instrumentation being required. Active sources have the advantage of higher frequencies, which give sharper arrival peaks, as well as controllability and continuous monitoring. Theoretical descriptions, simulated results, and experimental results, are presented for each case.

1.1 Gaps in the literature

A detailed discussion of literature relevant to this research is presented in **Chapter 2**. A conceptual explanation of the emergence of Green's function characteristics from cross-correlations, and an inter-disciplinary discussion of relevant cross-correlation literature, are presented. The chapter concludes with a more specific discussion of previous publications concerning Green's function estimation from cross-correlations in the ocean environment.

This thesis will address the following gaps in the literature which have been identified:

1. It has been shown theoretically using a modal approach in the frequency domain, and through simulation, that the Green's function between two receivers in a waveguide can be determined by summing the cross-correlations from a vertical line of sources that are located in the same vertical plane as the receivers, external to them [29]. Theoretical arguments based on the method of stationary phase have been used by others to formulate the time domain Green's function for time-averaged surface generated ambient ocean noise cross-correlation [15] and seismic interferometry [30]. Stationary phase arguments have not previously been applied to active source configurations in the ocean. In addition, detailed theoretical descriptions of horizontal active source configurations have not been considered previously.

   Stationary phase descriptions of both vertical and horizontal source configurations will be presented within this thesis. These theoretical formulations will be supported by simulations. This work is presented in Chapter 3.

2. It has been shown experimentally that for a ship track passing through the end-fire plane of a pair of hydrophones (i.e., the vertical plane containing the hydrophones), if sufficiently long time windows are used, then the signal from the end-fire location dominates the cross-correlation function [25]. An in-depth analysis of cross-correlations

from ship dominated ocean noise has not, however, previously been presented.

Results from cross-correlation of ship dominated ambient noise data will be presented and analysed in detail in this thesis. The arrival time structure of empirical Green's function approximations determined from these cross-correlations will be compared to that of simulated Green's functions. This work is presented in Chapter 5.

3. The first gap in the literature pertained to theoretical descriptions of Green's function approximation from cross-correlation of active noise sources. Experimental validation of the theory has not previously been presented.

An experiment in which a source is lowered vertically through the waveguide, and one in which a source is towed along a straight line towards an array, are described in this thesis. Results from these experiments are presented and compared with simulated results and theory in Chapter 6. The results are also compared and contrasted to those obtained from ship dominated ambient noise cross-correlations.

4. Acoustic travel times extracted from ambient noise cross-correlations have been used by others [27] for array localisation and synchronisation. Other practical applications for the extracted travel time data have not been explored.

A practical application of noise cross-correlation for the diagnosis of a multichannel ocean hydrophone array is derived and presented in Chapter 7 of this thesis.

1.2   Document structure

For the benefit of non-experts in the field of ocean acoustics, background ocean acoustic theory is provided in Section 1 of **Chapter 2**. The propagation of sound in the ocean and the associated governing equations are

introduced. A summary of how the Green's function can be derived from the wave equation for a simple point source is then presented, along with a discussion of the various numerical models that are used to solve the wave equation in realistic ocean environments. Section 2 of **Chapter 2** is a critical literature review that confirms the gaps in the literature outlined in the previous section.

Chapter 3 addresses the first gap in the literature. A stationary phase argument is used to describe the relationship between the stacked cross-correlations from a line of vertical sources, located in the same vertical plane as two receivers, and the Green's function between the two receivers. Theory and simulations demonstrate the approach and are in agreement with those of a modal based approach presented by others. Results indicate that the stacked cross-correlations can be directly related to the shaded Green's function, provided the modal continuum of any sediment layers is negligible. A horizontal source configuration can be used instead of a vertical column. The relationship between the summed cross-correlation for a horizontal line source configuration and the Green's function is given. If range independence is assumed, it is demonstrated that the Green's function can be approximated from cross-correlations of a horizontal hyperbolic towed source with its apex at a location horizontally between two physical hydrophones. The chapter concludes with a brief comparison of the three active source configurations.

In **Chapter 4** an overview of the Shallow Water 2006 (SW06) experiment is given. The direct acoustic path, that is, the acoustic path that does not interact with the sea surface and seafloor, is shown to be highly sensitive to changes in sound speed profile. This makes reflection coefficient inversion difficult, although attempts to do so suggest a critical angle and sediment sound speed in agreement with that estimated by others.

Chapter 5 addresses the second gap in the literature. Cross-correlation of ocean noise in the 20–100 Hz frequency range is discussed. Ocean noise data, collected by three L-shaped arrays during the SW06 sea tri-

als, were cross-correlated in order to approximate Green's functions, and subsequently acoustic travel times of the main propagation paths, between hydrophone pairs. Examination of the individual noise spectra and their mutual coherence reveals that the propagating noise is most coherent at ship noise dominated frequencies of less than 100 Hz. Both time and frequency domain preprocessing techniques, and their effect upon the cross-correlations, are investigated. Travel times corresponding to the envelope peaks of the noise cross-correlation time-derivatives are in agreement with the expected direct and surface reflected inter-hydrophone travel times. Summing the cross-correlations between equi-spaced hydrophone pairs in a horizontal line array (HLA) is shown to increase the signal-to-noise ratio. Temporal changes in short-time cross-correlations highlight individual ship tracks and show that the sound field is more diffuse during the passing of a tropical storm.

The third gap in the literature is addressed in **Chapter 6**. Cross-correlations obtained using two active source configurations (source lowering and towed source) are compared and contrasted with cross-correlations from a noise field dominated by shipping, and also with cross-correlations of noise generated during the source lowering event by the ship from which the source was being controlled. The various source configurations are investigated theoretically, and experimental results for each source type, from cross-correlation of data collected during the SW06 sea trials, are compared.

Chapter 7 details two practical applications of noise cross-correlation: the analysis of *channel switching* on an ocean hydrophone array, which addresses the fourth gap in the literature; and array element self-localisation, using a methodology similar to that of others [27]. Channel switching refers to the event where signals from a given hydrophone that were originally recorded on a certain channel are subsequently recorded on a different channel. Acoustic data were recorded on the horizontal portion of an array on the New Jersey Shelf during the passing of Tropical Storm Ernesto on September 2 2006. Results obtained from active source measurements prior to

and after the passing of the storm revealed that several channels switched during the storm. Noise cross-correlation of data recorded during the storm was performed, and changes in the cross-correlation showed when, and in what manner, the channel switching took place. In addition to the channel switching, it was noticed that travel times of acoustic data recorded on the array showed inconsistencies with the given array geometry; differences in travel times from any given source to HLA hydrophone pairs were consistently less than expected. It was therefore hypothesised that the HLA was not lying in a straight line on the seafloor. Travel times extracted from day long ambient noise cross-correlations, with the channel switching taken into account, are used in a non-linear least squares inversion to estimate array geometry. The resulting geometry is consistent with acoustic travel times of active acoustic sources.

Conclusions from the research are presented in **Chapter 8**. Possible directions for future work are outlined. Much of the work presented in this thesis has been either published or submitted for publication by the author in international journals and conference proceedings, as listed in Appendix D.

Chapter 2

Literature Review

This chapter is organised into two main sections: background ocean acoustic theory is presented in Section 2.1, and a critical review of the literature pertinent to the work in this thesis is presented in Section 2.2.

2.1 Background

In order to fully appreciate why one would want to "approximate the acoustic Green's function in the ocean via cross-correlation methods", one must first have a basic understanding of what the Green's function represents and hence why it is useful to obtain an approximation of it, as well as of the potential benefits of estimating the Green's function via cross-correlation as opposed to traditional methods.

The physical and chemical factors that affect how sound propagates in the ocean are described in Section 2.1.1. The equations that govern the propagation of sound: the acoustic wave equation, and its frequency equivalent, the Helmholtz equation, are subsequently introduced in Section 2.1.2. The Green's function between two points, defined as the solution to the Helmholtz equation at the second point given a unit impulse applied at the first point, is then introduced in Section 2.1.3. In simpler terms, the Green's function takes every little detail of the ocean environment into account, and

for any given sound source at one location, it specifies the signal that will be received at another location.

The Green's function can be derived theoretically from the acoustic wave equation for a simple source and geometric configuration, and a summary of the derivation for the example of a point source in an unbounded homogeneous medium is presented in Section 2.1.3. In more realistic ocean environments the governing boundary value problem becomes too complex to solve analytically, and numerical solutions are required. The most common types of numerical models used to generate solutions to the wave equation are briefly described in Section 2.1.4.

2.1.1 Propagation of sound in the ocean

The propagation of sound in the ocean is influenced by many factors including the physical and chemical properties of the water column, the structure and properties of the seafloor, and roughness at the sea surface interface.

Sound speed profile (SSP)

The speed of sound in water, c, is a function of static pressure (related to depth [31]), salinity, and temperature. A commonly used approximation for the relationship is [32]

$$c = 1449.2 + 4.6T - 0.055T^2 + 0.00029T^3 + (1.34 - 0.01T)(S - 35) + 0.016z,$$
$$(2.1)$$

where T is the temperature in degrees Celcius ($0 \leq T \leq 35°$ C), S is the salinity in parts per thousand ($0 \leq T \leq 45$ ppt), and z is the depth in metres ($0 \leq D \leq 1000$ m). More complex formulae for the relationship, which should be considered if high accuracy is needed, also exist [33, 34].

Temperature and pressure effects dominate salinity effects. In a shallow water environment the sound speed is generally either dominated by a negative thermocline, a thin layer in which temperature and hence sound speed decrease rapidly with depth, or is nearly constant over depth. The upper

surface layer (i.e., the layer above the thermocline) is highly susceptible to weather influences. Diurnal heating warms the ocean surface and wave action mixes this warmer water with underlying cooler water, yielding a surface layer of approximately uniform temperature and sound speed. Below this mixing layer the temperature decreases rapidly, resulting in a steep negative thermocline. At even greater depths pressure effects dominate, and the sound speed then increases slowly with depth.

The propagation of sound through the ocean is described by Snell's law:

$$\frac{\cos\theta}{c} = \text{constant}, \tag{2.2}$$

where θ is the ray angle relative to the horizontal and c is the local sound speed. Sound is therefore locally refracted towards regions of low sound speed. Shallow water environments with a strong negative thermocline are downward refracting, and hence long range acoustic propagation is dominated by bottom-interacting acoustic paths. At shorter ranges acoustic propagation will be a combination of direct, surface reflected, seafloor reflected, and multiple-reflected paths.

Spreading and attenuation losses

The amplitude of propagating sound decreases due to a combination of attenuation and spreading effects. Geometric spreading is dominated by spherical or cylindrical effects, while attenuation is dominated by volume absorption, bottom reflection loss, and scattering losses at the surface and seafloor.

Spherical spreading occurs when sound propagates away from a source uniformly in all directions. This type of model is valid in the near-field ($r \leq D$, where D is ocean depth) of point sources located away from the ocean waveguide boundaries. Consider sound spreading spherically from a sphere of radius r_0 to a larger sphere of radius r. The power radiates equally in all directions, and neglecting attenuation, remains constant with

range:

$$P = 4\pi r_0^2 I_0 = 4\pi r^2 I, \tag{2.3}$$

where I is the acoustic intensity. The transmission loss (TL) between two points due to spreading is defined by the ratio of the intensity at the second point with reference to the intensity at a radius of $r_0 = 1\,\text{m}$ from an acoustic source:

$$\text{TL} = -10\log_{10}\left(\frac{I}{I_0}\right) = 10\log_{10}\left(r^2\right) = 20\log_{10}\left(r\right). \tag{2.4}$$

Due to the upper and lower boundaries of the ocean, at ranges far from the source $(r \gg D)$ sound propagates with cylindrical wavefronts. The power across the wavefront becomes

$$P = 2\pi r_0 D I_0 = 4\pi r D I, \tag{2.5}$$

and the transmission loss is therefore

$$\text{TL} = 10\log_{10}\left(r\right). \tag{2.6}$$

Volume absorption is the dominant attenuation factor for a path that does not have any boundary interactions. It is caused by viscosity and chemical relaxation, and is dependent upon temperature, salinity, acidity, and frequency. Several algorithms exist for calculating absorption in a given environment. Fisher and Simmons [35] presented an equation that is valid for a standard salinity of 35 ppt and a pH of 8. Francois and Garrison [36] presented a more complex relationship that is valid for a greater range of water properties, and Ainslie and McColm [37] subsequently presented a simplified relationship that is also valid for a standard range of oceanographic conditions. An example of absorption plotted as a function of frequency [36] is shown in Figure 2.1. Volume absorption can be seen to increase significantly with frequency, and hence long range propagation is dominantly at lower frequencies.

Sound that interacts with the seafloor is governed by Eq. (2.2). The sound speed and density, and hence the characteristic acoustic impedance, ρc, of the sediment at the seafloor is usually significantly greater than within
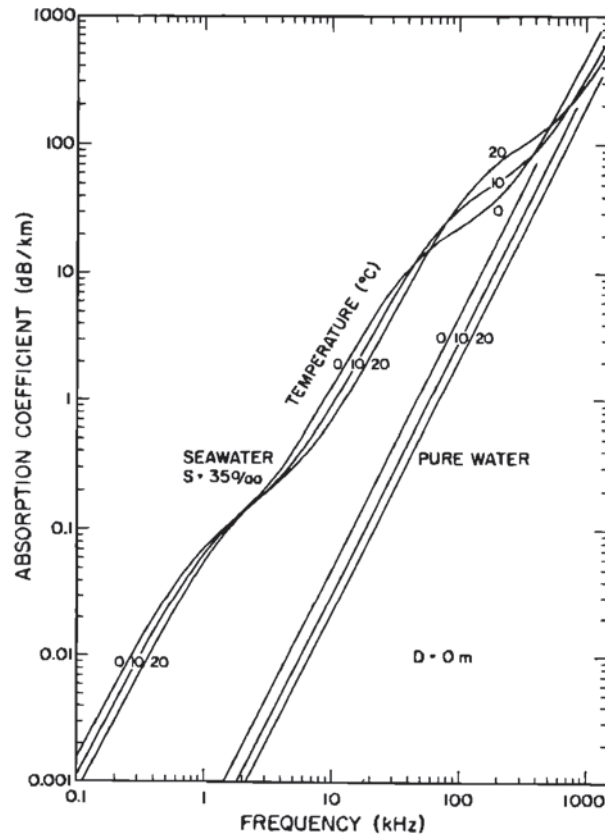
Figure 2.1: Absorption of seawater at three temperatures (°C) as a function of frequency for salinity of 35 ppt and pH of 8. Pure water attenuation is also shown as a reference (source: Francois and Garrison [36]).

the water column, and therefore the effect on acoustic propagation can be large. If the water is defined as medium 1 and the sediment as medium 2, Snell's law can be rewritten as $\frac{\cos\theta_1}{c_1} = \frac{\cos\theta_2}{c_2}$, where θ_1 is the horizontal angle, defined as the grazing angle, of the incident acoustic path, and θ_2 is the angle of the acoustic path in the second medium. In general, some of the incident acoustic energy is reflected from the interface with a reflection angle of θ_1, while some of the energy transmits to the sediment with a refraction angle of θ_2. The proportion of the energy that is reflected depends upon the ratio of impedances as well as the incident grazing angle. Since

13

$c2 > c1$, there exists a real valued grazing angle, defined as the *critical angle*, $\theta1 = \theta c$ = arccos($c1/c2$), below which $\theta2$ becomes complex. An acoustic path with a grazing angle less than or equal to the critical angle will therefore experience perfect reflection with an associated phase change. At angles above the critical angle, some of the energy is transmitted into the sediment; the steeper the grazing angle, the greater the transmission. Hence, at high grazing angles bottom reflection losses become the dominant loss mechanism. The bottom loss as a function of grazing angle for a typical environment [38] is shown in Figure 2.2.

NOTE: This figure is included on page 14 in the print copy of the thesis held in the University of Adelaide Library.

Figure 2.2: Bottom reflection loss versus angle for a non-lossy bottom, defined as a bottom with no p-wave attenuation, and also for a lossy bottom, defined as one with a high p-wave attenuation factor. (source: Jensen [38]).

Scattering is redirection of sound, through transmission, reflection, and diffraction, as it encounters an inhomogeneity. Sound in the ocean is scattered by roughness at both the sea surface and the seafloor. The amount of scattering increases with surface roughness, frequency, and grazing angle. The process of boundary scattering is physically complex and as such the literature is extensive (see Ogilvy [39] for a review). Volume scattering in the ocean occurs due to sound interaction with air bubbles, marine life and small-scale ocean structure such as internal waves (see Medwin and Clay [3] for a review).

2.1.2   Overview of the acoustic wave equation

Forward propagation models are based upon the acoustic wave equation. The wave equation in an ideal fluid stems from hydrodynamics and the adiabatic relationship between pressure and density. From the first order representation of the conservation of mass, Euler's equation, and the adiabatic equation of state, the linear acoustic homogeneous three-dimensional wave equation for pressure is derived to be [4]

$$\rho \nabla \cdot \left(\frac{1}{\rho} \nabla p \right) - \frac{1}{c^2} \frac{\partial^2 p}{\partial t^2} = 0, \tag{2.7}$$

where ρ is the density, p is the pressure, c is the speed of sound within the fluid, t represents time, $\nabla = \mathbf{i}(\partial/\partial x) + \mathbf{j}(\partial/\partial y) + \mathbf{k}(\partial/\partial z)$ is the del operator, and $\nabla \cdot \left(\frac{1}{\rho} \nabla p \right)$ is the divergence of $\left(\frac{1}{\rho} \nabla p \right)$. If density is assumed spatially constant, Eq. (2.7) simplifies to

$$\nabla^2 p - \frac{1}{c^2} \frac{\partial^2 p}{\partial t^2} = 0, \tag{2.8}$$

where ∇^2 is the *Laplacian*, which, in rectangular co-ordinates, is defined as $\nabla^2 = \nabla \cdot \nabla = \frac{\partial^2}{\partial x^2} + \frac{\partial^2}{\partial y^2} + \frac{\partial^2}{\partial z^2}$. Assuming time-harmonic waves where the pressure fluctuates sinusoidally with frequency, application of the Fourier transform to Eq. (2.8) yields the frequency domain form of the wave equation, the Helmholtz equation:

$$[\nabla^2 + k^2]p = 0, \tag{2.9}$$

where k is the wavenumber, defined as the ratio between frequency and sound speed:

$$k = \frac{\omega}{c}. \tag{2.10}$$

The linear homogeneous Helmholtz equations for velocity potential, ϕ, and displacement potential, ψ, are of the same form as Eq. (2.9), and are given by

$$[\nabla^2 + k^2]\phi = 0, \tag{2.11}$$

and

$$[\nabla^2 + k^2]\psi = 0. \tag{2.12}$$

15

2.1.3 Overview of the acoustic Green's function

The general Green's function, G, between two points, $\mathbf{r}$ and $\mathbf{r}_0$, is the signal that would be received at one point given a unit impulsive source at the other. It satisfies the inhomogeneous Helmholtz equation:

$$[\nabla^2 + k^2]G(\mathbf{r}, \mathbf{r}_0) = -\delta(\mathbf{r} - \mathbf{r}_0), \qquad (2.13)$$

where δ is the Dirac delta function. The general Green's function is therefore fully dependent upon the geometry and environment under consideration, and as such, can be used to determine information about the environment through which acoustic transmission between the two points takes place, in this case the ocean waveguide and the underlying sediment.

Green's function in an unbounded homogeneous medium

Consider an acoustic point source (vibrating sphere) in an unbounded medium as shown in Figure 2.3. A detailed derivation of the Green's function for this configuration is given by Jensen *et al.* [4] (pages 69–73). A summary of the more important concepts and equations is presented here.
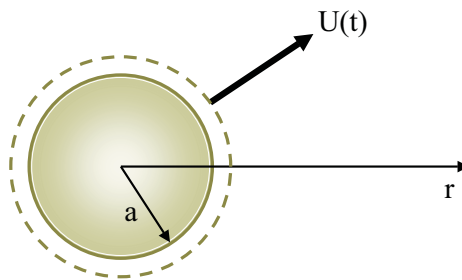

Figure 2.3: Vibrating sphere in an infinite fluid medium (source: MIT OCW [40], adapted from Jensen *et al.* [4]).

For a homogeneous point source in a spherical co-ordinate system, the homogeneous Helmholtz field equation, Eq. (2.12), reduces to

$$\left[\frac{1}{r^2} \frac{\partial}{\partial r} r^2 \frac{\partial}{\partial r} + k^2 \right] \psi(r) = 0, \qquad (2.14)$$

which has two linearly independent solutions:

$$\psi(r) = \begin{cases} (A/r)e^{ikr} \\ (B/r)e^{-ikr}, \end{cases} \tag{2.15}$$

where A and B are constants. The two solutions represent outward- and inward-propagating spherical wave solutions respectively, with time dependence $\exp(-i\omega t)$.

Consider a small sphere of radius a with surface displacement $u(t, a) = U(t)$, or in the frequency domain $u(a) = U(\omega)$. The radial displacement of the field is

$$u(r) = \frac{\partial \psi(r, t)}{\partial r}. \tag{2.16}$$

By considering Eq. (2.15) and Eq. (2.16) together, incorporating the surface displacement boundary condition, and using the $ka \ll 1$ approximation, the amplitude of the outward propagating solution to the displacement potential, the first solution of Eq. (2.15), is determined to be $A = -a^2 U(\omega)$. The displacement field becomes

$$\psi(r) = -S(\omega)\frac{e^{ikr}}{4\pi r}, \tag{2.17}$$

where $S(\omega) = 4\pi a^2 U(\omega)$ is the volume source strength.

The Green's function, g, is the field solution, Eq. (2.17), for an impulse input, $S(\omega) = -1$:

$$g(r, 0) = \frac{e^{ikr}}{4\pi r}, \tag{2.18}$$

which, for a source at $\mathbf{r} = \mathbf{r}_0$, generalises to

$$g(\mathbf{r}, \mathbf{r}_0) = \frac{e^{ikR}}{4\pi R}, \tag{2.19}$$

where $R = |r - r_0|$.

Green's function in a homogeneous environment

The Green's function, $g(\mathbf{r}, \mathbf{r}_0)$, of Eq. (2.19) is a particular solution to Eq. (2.13) that satisfies the free-field radiation condition. In a bounded

medium such as an ocean waveguide, the general Green's function, G, satisfying Eq. (2.13), is the sum of a particular solution, g, and a homogeneous solution, H:

$$G(\mathbf{r}, \mathbf{r}_0) = g(\mathbf{r}, \mathbf{r}_0) + H(\mathbf{r}), \tag{2.20}$$

where H satisfies the homogeneous Helmholtz equation:

$$[\nabla^2 + k^2]H(\mathbf{r}) = 0. \tag{2.21}$$

Analytical solutions for the general Green's function can be determined for simple environments such as a source in a fluid halfspace [4, 41].

2.1.4   Numerical solutions to the wave equation

Although the wave or Helmholtz equation can be solved theoretically for simple environments such as an acoustic point source in an unbounded medium, numerical models need to be employed to generate a solution for more complex environments. One of four numerical methods are typically used to solve the Helmholtz equation: ray theory, wave number integration, normal modes, and parabolic equation approaches. The time-domain wave equation can be solved using finite differences or finite elements.

The assumptions upon which a numerical method is based determines the complexity of the environment to which it can be successfully applied. Range independent environments are those with environmental parameters that are invariant with range. They are commonly referred to as *horizontally stratified* environments and can be modelled using any of the numerical methods. Range dependent environments are those in which the environmental parameters are not assumed to be constant with range. Only numerical methods that do not assume horizontal stratification can be successfully applied to these more complex environments.

Although many environments can be considered close to horizontally stratified, there exist numerous situations in which this assumption cannot be made. Environments that exhibit significant variations in the sound speed profile as a function of range, such as oceanic fronts, must be treated

as range dependent. Variations in seafloor bathymetry, such as sea mounts, and intrusions of basement material, such as uplifted faults, must also be analysed using a range dependent model.

Ray methods

Ray theory uses ray tracing methods to calculate the transmission loss through the fluid medium. The solution to the Helmholtz equation is assumed to have amplitude and phase components. The surfaces of constant phase are the wavefronts and the normals to these are the rays.

The rays passing through any specific point, termed the *eigenrays*, are a combination of direct rays and those experiencing boundary reflections. The pressure field at a point is the sum of the complex pressures of the eigenrays.

Ray methods use a geometrical acoustic approximation that limits them to the high frequency domain. In general, they are accurate in situations where the acoustic wavelength is smaller than any physical scale in the problem.

Although conceptually simple, ray methods are mathematically complex and hence 1-Dimension or 2-Dimension versions are generally preferred over 3-Dimension versions. The theory can be applied to range dependent applications using various range-partitioning techniques as discussed in the literature [5].

Ray methods experience difficulties in the vicinity of shadow zones and caustics, which are formed due to the refractive properties of the ocean environment focussing a number of adjacent rays into very close proximity. To eliminate the difficulties resulting from this, Gaussian beam tracing, which incorporates beamwidth and curvature equations, can be used [42, 43]. Shadow zones are regions through which no real-valued eigenrays pass; however, in practice sound will still pass through these regions. To overcome this anomaly, complex eigenrays need to be accounted for in the problem. Ray models assume specular reflection with a certain bottom reflection loss.

In reality the seafloor is not specular. Sound may be scattered, absorbed, refracted, attenuated, and then transmitted back into the water column at another location. Modifications to basic ray theory need to be made to overcome this [4, 5].

The advantages of ray models over other forward modelling techniques are that they are quick, intuitive, and ideal for obtaining arrival structure information, which is important for computing the directionality of ambient noise. The main disadvantage is that they are difficult to accurately apply to low frequency situations.

Wavenumber integration techniques

Wavenumber integration is a numerical implementation of the integral transform technique for range independent media [4]. The assumption of range independence means that the coefficients of the Helmholtz equation and the boundary conditions will be independent of the range coordinates. The dimensions of the wave equation and boundary conditions can therefore be reduced through use of integral transforms (separation of variables), yielding the *depth-separated wave equation*. Numerous different quadrature schemes for solving the depth-separated wave equation, such as direct trapezoidal integration, with varying degrees of versatility and numerical stability, exist. Jensen *et al.* [4] discusses the more common schemes in detail.

Wavenumber integration has the advantages of being accurate in the near field and valid at all frequencies. The main disadvantages are that it is computationally inefficient to apply to range-dependent environments, and correct application of the technique requires considerable user expertise.

Normal modes

The normal mode method has the same mathematical basis as wavenumber integration. The difference is that an unforced version of the depth-separated wave equation is initially assumed [4]. The unforced equation

has a set of resonant modes, analogous to the modes of vibration of a simple beam. The modes are characterised by a mode shape function, an eigenfunction, and a propagation constant analogous to a beam resonance frequency, an eigenvalue. Taking the source pressure into account, the complete acoustic field is constructed by summing the contributions of each mode (sum of the residues), weighted in accordance with the source depth. The accuracy of the solution is strongly dependent on the number of modes assumed for computational purposes, and hence a number of modes sufficient to achieve solution convergence should be used. Extension of the normal modes method to range dependent problems can be achieved through mode coupling, which is computationally demanding, or through adiabatic approximation [5].

Normal modes have the advantage of computational efficiency and high accuracy at low frequencies. Their main disadvantage is that they are not completely accurate for near field computations.

Parabolic equations

The implementation of parabolic equations is the most popular method for solving range dependent underwater propagation problems [4]. The Helmholtz equation, Eq. (2.9), is rewritten in cylindrical co-ordinates:

$$\frac{\partial^2 p}{\partial r^2} + \frac{1}{r}\frac{\partial p}{\partial r} + \frac{\partial^2 p}{\partial z^2} + k_o^2 n^2 p = 0, \tag{2.22}$$

where $k_o = \omega/c_o$ is the reference wavenumber and $n = c_o/c$ is the refraction index. A solution of the form

$$p(r, z) = \Psi(r, z) S(r), \tag{2.23}$$

is assumed, where $\Psi(r, z)$ is an envelope function and S is a range dependent function. The assumed solution is substituted back into Eq. (2.22) and separation of variables is applied, yielding

$$\frac{\partial^2 S}{\partial r^2} + \frac{1}{r}\frac{\partial S}{\partial r} + k_o^2 S = 0, \tag{2.24}$$

and

$$\frac{\partial^2 \Psi}{\partial r^2} + \left(\frac{1}{r} + \frac{2}{S}\frac{\partial S}{\partial r}\right)\frac{\partial \Psi}{\partial r} + \frac{\partial^2 \Psi}{\partial z^2} + k_o^2 n^2 \Psi - k_o^2 \Psi = 0. \qquad (2.25)$$

Equation 2.24 is a first order Bessel equation, the solution of which is a first order Hankel function:

$$S = H_o^{(1)}\left(k_o r\right). \qquad (2.26)$$

Using a far-field approximation, $k_o r \gg 1$, Eq. (2.26) simplifies to

$$S \approx \sqrt{\frac{2}{\pi k_o r}} e^{i(k_o r - \pi/4)}. \qquad (2.27)$$

Substituting Eq. (2.27) into Eq. (2.25) and simplifying yields

$$\frac{\partial^2 \Psi}{\partial r^2} + 2ik_o\frac{\partial \Psi}{\partial r} + \frac{\partial^2 \Psi}{\partial z^2} + k_o^2 n^2 \Psi - k_o^2 \Psi = 0. \qquad (2.28)$$

Introducing the paraxial approximation, which assumes that the contribution from the second radial partial derivative is negligible, yields the *standard parabolic equation*:

$$2ik_o\frac{\partial \Psi}{\partial r} + \frac{\partial^2 \Psi}{\partial z^2} + k_o^2\left(n^2 - 1\right)\Psi = 0. \qquad (2.29)$$

The parabolic equation can be applied to range dependent environments. It has the computational advantage over the elliptic reduced wave equation in that it is a one-way wave equation that can be solved by a highly efficient range-marching solution technique using a range step greater than the acoustic wavelength. The main disadvantage of parabolic equations is that their application requires considerable user expertise.

Numerous different numerical means of solving the parabolic equation exist. These are discussed in detail in the literature [4, 5, 44, 45]. Standard parabolic equation methods have an intrinsic problem with energy conservation. Energy loss can occur in propagation up a positive slope, whilst energy gain can occur in propagation down a slope. This is due to the slope being considered as a finite number of horizontally stratified segments, with discontinuous boundaries. To overcome the energy conservation problem either the interface conditions need to be selected carefully, or a direct sloping-boundary condition can be implemented [46].

Finite differences and finite elements

Finite differences and finite elements are usually implemented in the time domain. The finite difference method discretises the inhomogeneous wave equation in space and time. The finite element method discretises the environment into regions within which the inhomogeneous wave equation can be solved analytically, resulting in a linear system of equations. Both methods, which are geometrically flexible, can provide highly accurate solutions, as generality is not sacrificed through assumptions and approximations. If a pulse source is assumed, the energy partitioning of the wave field, that is, the form and location of the acoustic energy, can be determined as a function of time [47]. From this, insight into the physical propagation effects can be obtained. An excessively large computation effort is required. The field coefficients at each grid point into which the governing wave equation (finite differences) or physical domain (finite elements) is discretised, are stored in matrices, which tend to be large, and it is the inversion of these large matrices that requires intensive computation. Finite differences and elements are therefore usually just used for providing benchmark solutions to a problem.

Numerical solutions used in this thesis

Ray tracing and wavenumber integration are the two numerical techniques for solving the acoustic wave equation used in this thesis. Bellhop [48] ray tracing software is used for path visualisation because ray tracing is fast, intuitive, and the results are easily visualised. The environments considered here are assumed range independent and propagation is over a short range and wide frequency band. OASES (*Ocean Acoustics and Seismic Exploration Synthesis*) wavenumber integration software [49] was therefore considered ideal for all other modelling.

2.2 Literature review on Green's function extraction

Within this section the theory of cross-correlation is introduced. The earliest works showing that the Green's function between two points can be determined from their temporal cross-correlation are described in Section 2.2.1, and the theory of why this is true is presented in Section 2.2.2 for cross-correlations in a uniform homogeneous medium. Further inter-disciplinary works in Green's function extraction are then reviewed in Section 2.2.3.

A conceptual argument relating the cross-correlation of surface sources to the Green's function between two points in a waveguide is presented in Section 2.2.4. This chapter concludes with Section 2.2.5, a discussion of recent literature describing Green's function approximation from cross-correlations of sound in the ocean.

2.2.1 Early research on Green's function extraction from cross-correlations

It was shown theoretically many years ago [50, 51] that under certain conditions the auto-correlation of an earthquake seismogram mimics the echo of an explosive at the correlation location. From this theory, it was hypothesised that the cross-correlation of noise traces at two different locations was related to the Green's function between these locations [52]. Before this was conclusively shown on Earth, Duvall Jr *et al.* [53] showed that time-distance information could be extracted from temporal cross-correlations of the intensity fluctuations on the solar surface. Farrar and James III [54] related the cross-correlation of two response measurements on an ambiently excited structure to the Green's function of the system.

2.2.2 Conceptual description of cross-correlations in a uniform homogeneous medium

Temporal correlation is a measure of the degree of similarity between two signals as a function of time. The comparison of a signal with a time-lagged version of itself is termed *auto-correlation*, while the comparison of two different signals is termed *cross-correlation*.

It has been shown [13, 16, 55] that for a homogeneous medium with sound speed c, the cross-correlation of a uniformly distributed broadband sound field recorded at two receivers separated by distance L, is continuous for $|t| < L/c$, noncontinuous at $t = \pm L/c$, and zero for $|t| > L/c$. A graphical explanation of this is presented here.

The cross-correlation of signals recorded at receivers A and B, as a function of time delay τ, is defined as

$$C_{AB}(\tau) = \int_{-\infty}^{\infty} P(\mathbf{r}_A, t) P(\mathbf{r}_B, t + \tau) dt, \tag{2.30}$$

where P is pressure, $\mathbf{r}_A$ and $\mathbf{r}_B$ are the locations of receivers A and B with respect to an origin, and t is time. The free-field cross-correlation of a broadband signal from an impulse source at location $\mathbf{r}_s$ will therefore be an impulse at time delay

$$\tau = \frac{|\mathbf{r}_B - \mathbf{r}_S| - |\mathbf{r}_A - \mathbf{r}_S|}{c} \leq \frac{L}{c}. \tag{2.31}$$

Sources that yield a cross-correlation at the same time delay therefore lie on a hyperbola with its focus at one of the receivers and its asymptotes intersecting mid-way between the receivers.

The cross-correlations from various source impulse locations are shown in Figure 2.4. The source/receiver geometries are shown on the left with their corresponding cross-correlations to the right according to the following: (a) a source impulse from anywhere along the line perpendicular to the A-B axis, and equi-distant from A and B, will be received at both A and B simultaneously; and (b) the cross-correlation will therefore yield an impulse with zero time delay. In (c) a source located on the A-B axis closer

to A and external to the sources is received at B at a time L/c after it is received at A and hence yields (d) a cross-correlation at $\tau = L/c$. In (e) any other source that is received at A prior to B yields (f) a cross-correlation at a time delay of $0 < \tau = (L - 2(|A| - |x|))/c < L/c$. In (g) summation of cross-correlations from sources that span the region from $\tau = 0$ through $\tau = L/c$ yields (h) a boxcar function. In (i) inclusion of sources that are received at B before A (j) fills in the acausal side of the cross-correlation. Figure 2.4 only shows sources on a semi-ellipse, but due to symmetry a full ellipse produces an identical response.

The boxcar function and its derivative

$$\frac{dC}{dt} = -\delta(t - L/c) + \delta(t + L/c), \qquad (2.32)$$

are shown in Figure 2.5. The cross-correlation derivative is seen to be proportional to the sum of the causal and acausal Green's functions:

$$\frac{dC}{dt} = -G(t) + G(-t). \qquad (2.33)$$

Realistically a band-limited signal is recorded and correlated. A 0.05– 0.2 Hz filtered cross-correlation and its time derivative are also shown in Figure 2.5. Note that the cross-correlation rapidly drops to near zero at times less than the inter-receiver travel time. The band-limited signal does not have a zero-frequency component and therefore the phase characteristics result in peaks in the cross-correlation that do not correspond to peaks in the Green's function destructively interfering with one another. The band-limited cross-correlation time derivative has a waveform like structure. The peak of this occurs at the same time as for the simplified broadband case. An isotropic noise distribution yields a symmetric cross-correlation; a one-sided distribution would give an approximation of only the causal Green's function.

The general relationship between the cross-correlation function and the Green's function is

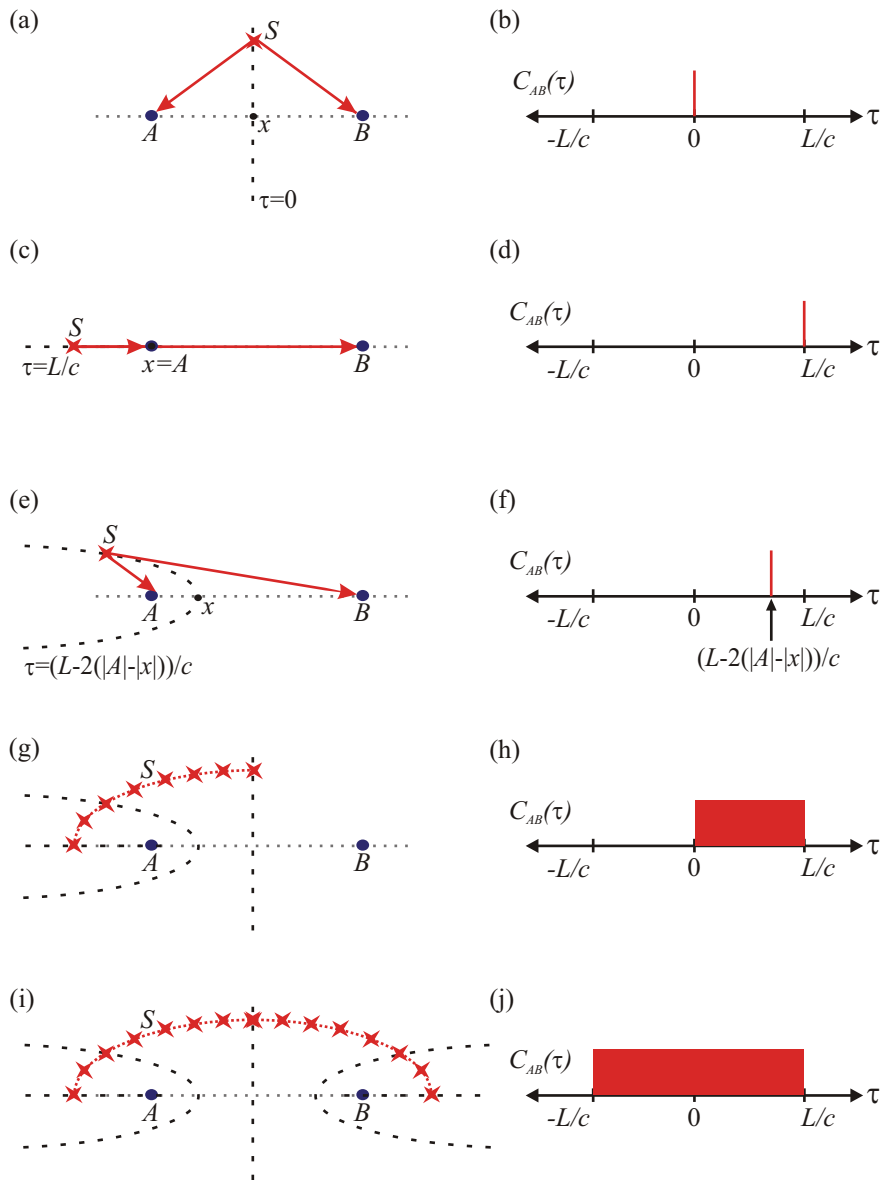$$-\frac{dC}{dt} \simeq G(t) - G(-t). \qquad (2.34)$$

Figure 2.4: Cross-correlation of a source impulse in free space. Figure details are described in the main text.

NOTE: This figure is included on page 28 in the print copy of the thesis held in the University of Adelaide Library.

Figure 2.5: Free-field cross-correlation examples. Top to bottom: broadband noise correlation function (NCF), derivative of the broadband NCF, filtered (0.05–0.2 Hz) NCF, and derivative of the filtered NCF (adapted from Gerstoft *et al*. [16]).

Equality is not absolute in Eq. (2.34). Reasons for this will be discussed in Section 3.1.1.

2.2.3 Interdisciplinary review of Green's function extraction from cross-correlations

Approximation of the Green's function between two points in both open and closed environments has been more widely studied since Lobkis and Weaver [7] showed, both theoretically and experimentally, that an approximation of the Green's function between two points can be determined from their temporal cross-correlation within a diffuse ultrasonic field. Their experimental arrangement and results, as shown in Figure 2.6, are briefly described here as they provide a simple explanation of the general concepts governing the extraction of Green's functions from noise cross-correlations. A broadband (0.1–0.9 MHz) ultrasonic impulse was input to an aluminium block at point **s**. Due to the irregular block shape, a long-time pseudodiffuse field was created. The pseudo-diffuse field was measured at two receivers, **x** and **y**, and cross-correlated. The cross-correlation was then compared to the Green's function between receivers **x** and **y**, obtained by measuring the signal received at **y** from an impulsive input source at **x**.

The cross-correlated field and the Green's function show good agreement, but there are discrepancies, particularly in amplitude.

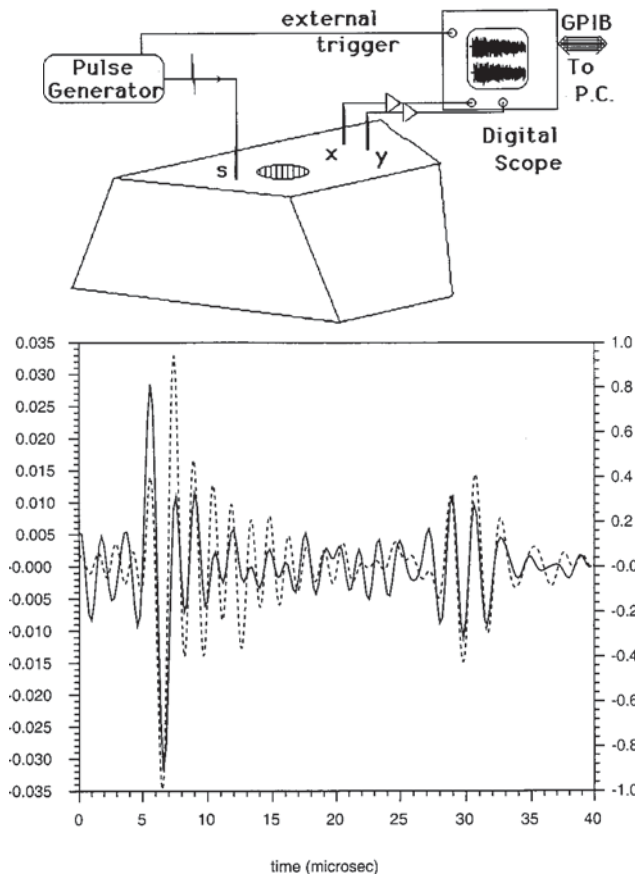Figure 2.6: (top) Impulse source creates pseudo-diffuse field in a block, which is detected at receivers **x** and **y**; (bottom) the cross-correlation of the signals (solid line) is compared to the signal (dashed line) which would be received at **y** given an impulse source at **x** (source: Lobkis and Weaver [7]).

A *diffuse* field is one in which the modal amplitudes are uncorrelated random variables. Although the block specimen was irregular, it was not lossless, and hence a source input at only one location would not precisely satisfy the diffuse field requirement, explaining why only a *pseudo-diffuse* field was created experimentally. The theory of Lobkis and Weaver explained how the relationship between the cross-correlation and Green's function is dependent upon the work done by the source on each mode, and hence am-

29

plitude equality will not be obtained if the diffuse field requirement is not met. They showed that increased temporal averaging and increased spatial averaging through the use of multiple source locations results in a field that more closely satisfies the diffuse field requirement, and therefore decreases the discrepancies between the cross-correlation and the Green's function.

The concepts of Lobkis and Weaver [7] were extended by Derode *et al.* [56] who showed that the Green's function can be conditionally recovered in an open scattering medium. They concluded that although the Green's function can be determined from cross-correlations from a single source within a lossless closed cavity in which it is assumed that the eigenmodes do not degenerate, the Green's function will only emerge from cross-correlations within an open scattering medium if they are summed over a perfect time-reversal mirror. Wapenaar [57] and Van Manen *et al.* [58] demonstrated that retrieval of the Green's function through summed cross-correlations can also be achieved in an inhomogeneous medium.

Extraction of the Green's function by cross-correlation has been applied to practical applications not just in helioseismology, structural engineering and ultrasonics, but also in other fields. In addition to the works of Lobkis and Weaver [7] and Derode *et al.* [56], numerous other significant contributions in cross-correlations of ultrasonic diffuse wavefields exist [8–10, 59]. Extensive studies on cross-correlations of ambient seismic noise have been presented [12–15, 17–19, 60, 61]. Curtis *et al.* [28] published an extensive review paper on seismic noise cross-correlation, and Bensen *et al.* [62] included a comprehensive review and comparison of existing seismic noise data processing techniques in their work. Green's function estimates from noise have also been applied to structural health monitoring [63], moon seismic noise [20], and human skeletal muscle noise [21].

2.2.4 Conceptual description of cross-correlations in a simplified isovelocity ocean waveguide

In its most general form the ocean can be considered as a waveguide bounded by a free-surface above and the seafloor below. If spreading and attenuation losses are ignored, an impulse source signal at location A will be recorded at a second location B as an infinite set of impulses at time lags that correspond to the acoustic travel paths between A and B. Consider the first three arrivals only: the direct path, surface reflected path, and bottom reflected path. The order of arrival of the latter two depends upon the locations of A and B. These three paths and the corresponding arrivals recorded at B are shown in Figure 2.7(a).

NOTE:
This figure is included on page 31
of the print copy of the thesis held in
the University of Adelaide Library.

Figure 2.7: Waveguide without losses. (a) Green's function between receivers A and B showing direct (red), surface reflected (green), and bottom reflected (blue) paths with corresponding Green's function shown to the right. (b)–(c) Surface sources that yield (b) direct path, and (c) direct and single reflected paths, with corresponding cross-correlations shown at the far-right (adapted from [64]).

The ocean sound field is dominated by sources at or near the surface. Surface sources that are received by both A and B with a lag time equal to the direct path travel time are shown in Figure 2.7(b). Note that for the lag time to be correct, the ray path from the sources must pass through both

receivers. The cross-correlation of these sources at A and B is an impulse at the direct path arrival time. All surface sources that contribute to the first three arrivals are shown in Figure 2.7(c).

The sources that sum constructively in the Green's function approximation do not span the ocean surface uniformly. If ocean surface noise is assumed to be uniform in generation, signals from sources whose paths do not contribute to Green's function time lags will be recorded and correlated. These cross-correlations would, by themselves, yield an arrival at an incorrect time; however, if a uniform band-limited source field exists, all of the cross-correlations from source signals that do not pass through both receivers cancel due to destructive phase interference. The finer mathematical details of why this occurs are too extensive to present here; however, a detailed stationary-phase theoretical explanation of this concept is presented in Sections 3.1.1, 3.1.2, and 3.1.3.

2.2.5 Review of Green's function extraction from cross-correlations in the ocean

Realistic ocean environments are far more complex than the generalised environment considered in Section 2.2.4. Refraction within the water column and at the water-sediment interface, spreading and attenuation losses, and uneven source distributions, mean that Green's function approximation is not as straightforward as the conceptual argument presented here may suggest. Several papers that have investigated important concepts relating cross-correlations in realistic ocean environments are discussed here.

Roux and Fink [29] showed theoretically and through simulation that the Green's function between two points can be determined by summing either the cross-correlations from a vertical line of sources that are located in the same plane as the two receivers, external to the two receivers, or from summing the convolution of the signals received from a vertical line of sources located co-planar between the two receivers. Their theory is based upon three main assumptions: the medium of interest is reciprocal

(i.e., fluctuations of the signal due to changes in the channel environment, such as currents or internal waves, can be assumed to be negligible); modal orthogonality holds (i.e., the water column contains sufficient sources that span the entire water column and density gradients are negligible); and the modal continuum of the acoustic bottom can be neglected (i.e., the range between the two receivers is sufficiently large). Using time-reversal, they compared back-propagated fields generated by the estimated Green's function with those generated by the exact Green's function and concluded that for both range independent and range dependent environments:

- the size and location of the focal point is virtually independent of source spacing;

- the spatial and temporal side-lobes within the back-propagated signal are suppressed sufficiently if the depth between successive sources is not greater than the smallest wavelength of the source spectrum;

- the focal spot is distorted if the sources do not span the entire water column;

- if there are insufficient sources, modal orthogonality does not hold and the estimated Green's function is erroneous in both phase and amplitude; and

- even if there are sufficient sources within the water column, the phase term of the estimated Green's function will be correct, but the amplitude term will remain erroneous.

Sabra *et al.* [15] presented theory and simulations demonstrating the relationship between time-averaged cross-correlations of noise generated at the sea surface by wave processes, and the Green's function between two hydrophones. Sabra *et al.* [27] also correlated noise from 150–700 Hz experimental noise data. Their sound field was dominated by croaker fish rather than surface generated noise, but due to the near isotropic distribution of the fish, they were able to obtain good estimates of the direct path travel

33

times between elements of a bottom mounted hydrophone array. They used these times to perform array self-localisation and self-synchronisation.

Using a vertical array of hydrophones, ocean noise cross-correlation has been used to approximate seafloor structure via passive fathometry [65, 66]. If the noise source is assumed to be completely uncorrelated surface noise, the estimated layer profile has been shown to have amplitudes that are proportional to those of an echo sounder at the same depth as the array [67].

Roux *et al.* [25] theoretically investigated the relationship between the time-averaged cross-correlation function and the Green's function for volume and surface sources as well as shipping noise. Their simulations of the cross-correlation function for the surface noise model agreed with the temporal structure of the Green's function. Roux *et al.* [25] also showed experimentally that if sufficiently long cross-correlation time windows are used, for a single ship track passing through the end-fire plane, which is defined as the plane containing the hydrophone array, of a pair of hydrophones, the signal from the end-fire location dominates the cross-correlation function. They presented simulations for sources located at various distances along the end-fire direction from the hydrophones and showed that the resulting summed cross-correlation peaks emphasised different parts of the Green's function, depending on the source range. From this they concluded that if a sufficiently large collection of random events is recorded, the structure of the complete Green's function can be obtained.

The works described in this section all further the understanding of Green's function extraction from ocean noise cross-correlation. The gaps in the literature identified in Section 1.1 are not due to weaknesses in previous works, rather the field of ocean acoustic interferometry is young, and many ideas have therefore yet to be fully explored.

Chapter 3

Active Source Ocean Acoustic Interferometry Theory

Using a stationary phase argument, this chapter explores the relationship between cross-correlations from active source configurations to two receivers within a waveguide, and the time domain Green's function between the two receivers. This approach is termed active source ocean acoustic interferometry (OAI), as it is related to classical and seismic interferometry [28], where interferometry refers to the determination of information from the interference phenomena between pairs of signals. The theoretical formulations and simulations presented here provide a basis for understanding active source OAI, and will be useful for explaining experimental results in Chapter 6.

The method of stationary phase is applied to simple reflective water column environments, providing an alternative theoretical means of describing and understanding the physics governing the cross-correlation of such a source configuration, and how this can be used to extract an amplitude shaded time domain Green's function (i.e., a Green's function convolved with amplitude factors). This work is distinct from work presented by Roux and Fink [29], Sabra *et al.* [15], and Snieder *et al.* [30], in that a stationary phase derivation is applied here to a vertical column of sources in a waveguide. A detailed physical and mathematical discussion of spurious ar-

rivals obtained in connection with OAI is presented. Numerical simulations of these environments support the theory. A refractive environment with more realistic water column, sediment, and bottom parameters is also analysed through numerical simulations. Although these geometrically simple scenarios are chosen as they allow for easier understanding of the results, the underlying concepts are also applicable to complex environments. Both the unstacked (unsummed) cross-correlations as a function of depth and the stacked (summed over depth) cross-correlations are analysed. The effect of limiting the sources to the water column is discussed and it is shown that the accuracy of OAI increases if the source column is extended through the sediment. The spurious arrivals obtained here are compared with those obtained by Sabra *et al.* [15] and Snieder *et al.* [30]. The manifestation of these aberrations are distinct in each case and these differences are explained by considering the different environments and geometrical set-up used in each case.

Three specific source configurations are introduced and explained: vertical source column, horizontal straight line towed source, and horizontal hyperbolic towed source.

A significant proportion of the work in this chapter has been published by the author in a 2007 journal paper [26].

3.1   Vertical source column

Consider the waveguide depicted in Figure 3.1. The x, y and z directions are defined as the horizontal axis, the axis in-and-out of the page, and the vertical axis, respectively. A vertical plane of sources spanning the water column (i.e., the z-direction) and extended towards infinity in the y-direction, and spaced sufficiently close to one another such that the highest-order mode that significantly contributes to the Green's function is sufficiently sampled, would form a perfect time-reversal mirror, meeting the requirements for determination of the Green's function between two points via cross-correlation

methods [29, 56]. However, it has previously been shown that only sources in the end-fire plane, that is, the same vertical plane as the two receivers (in Figure 3.1 this is the plane of the page), will contribute significantly to the cross-correlation

An expression for the cross-correlations of the signals received at two locations A and B, from a vertical column of sources, has previously been derived by Snieder *et al.* [30]. A summary of this derivation, adapted to the geometry being considered, is presented here. The signals from a set of sources received at A and B are

$$
\begin{aligned}
u_A(\omega) &= \sum_S \rho_s G(\mathbf{r}_A, \mathbf{r}_S) S_S(\omega) \\
u_B(\omega) &= \sum_{S'} \rho_{s'} G(\mathbf{r}_B, \mathbf{r}_{S'}) S_{S'}(\omega),
\end{aligned}
\tag{3.1}
$$

where ρ_s is the density of the acoustic medium, in this case the water column, at the source, S, $G(\mathbf{r}_\psi, \mathbf{r}_S)$ is the full Green's function between the source and receiver ψ, where $\psi = A$ or B, and $S_S(\omega)$ and $S_{S'}(\omega)$ are complex frequency source spectra of sources S and S' respectively. Cross-correlating the two expressions in Eq. (3.1) yields

$$
C_{AB}(\omega) = \sum_{S,S'} \rho_s \rho_{s'} G(\mathbf{r}_A, \mathbf{r}_S) G^*(\mathbf{r}_B, \mathbf{r}_{S'}) S_S(\omega) S_{S'}^*(\omega),
\tag{3.2}
$$

where * denotes the complex conjugate. If it is assumed that the sources are uncorrelated, the cross-terms, $S \neq S'$, equate to zero, and hence Eq. (3.2) simplifies to

$$
C_{AB}(\omega) = \sum_S \rho_s^2 G(\mathbf{r}_A, \mathbf{r}_S) G^*(\mathbf{r}_B, \mathbf{r}_S) |S(\omega)|^2.
\tag{3.3}
$$

For a vertical line of sources that is uniformly distributed (source spacing $\leq \lambda_{min}$) within the vertical plane containing receivers A and B, external to the two receivers, and closer to B, the cross-correlation becomes:

$$
C_{AB}(\omega) = |\rho_s S(\omega)|^2 n \int_0^D G(\mathbf{r}_A, \mathbf{r}_S) G^*(\mathbf{r}_B, \mathbf{r}_S) \, dz,
\tag{3.4}
$$

where n is the number of sources per unit length. The lower bound of the integral is 0 since the waveguide has a free surface at $z = 0$ and the upper

bound is the waveguide depth, D, since there are no reflective surfaces below this depth. This summed cross-correlation can, in the time domain, be determined from real or simulated data by calculating the cross-correlation for each source depth and then summing (also known as 'stacking') the result. The sum of the cross-correlations is related to the Green's function between A and B. This relationship is derived here for reflective environments using the method of stationary phase [68].
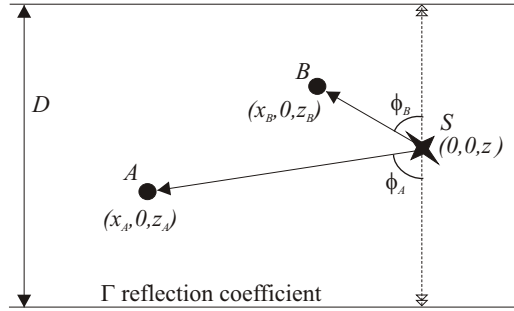

Figure 3.1: Source-receiver geometry and notation: the source S is located at $(0,0,z)$, and receivers A and B are located at $(x_A,0,z_A)$ and $(x_B,0,z_B)$ respectively within a waveguide of depth D.

The 3D Green's function within a homogeneous medium is [4]

$$G_f(R) = \frac{e^{ikR}}{4\pi R} \, , \tag{3.5}$$

where k is the wave number and R is the distance from the source. The full Green's function at each receiver can be written as the superposition of the direct and reflected waves. If the medium is an isovelocity waveguide, bounded above by a free surface and below by a reflective bottom with amplitude reflection coefficient Γ, the Green's function between the source, S, and receiver, ψ, is written in terms of the waveguide and source-receiver geometry [1] as

$$\begin{aligned}
G(\mathbf{r}_\psi, \mathbf{r}_S) = {} & \sum_{b_\psi=0}^{\infty} \Gamma^{b_\psi} G_f \left(\sqrt{x_\psi^2 + (2b_\psi D + z \pm z_\psi)^2} \right) \\
& + \sum_{b_\psi=1}^{\infty} \Gamma^{b_\psi} G_f \left(\sqrt{x_\psi^2 + (2b_\psi D - z \pm z_\psi)^2} \right),
\end{aligned} \tag{3.6}$$

where b_ψ is the number of bottom bounces for a given path, and D is the depth of the waveguide. The first term on the RHS includes all up-going waves and the second term includes all down-going waves as measured from the source.

Inserting Eq. (3.6) into the summed cross-correlation, Eq. (3.4), yields an expression for the cross-correlation that consists of the sum of the integrals of all possible combinations of the interaction between any path to the first receiver and any path to the second. Although the cross-correlation includes the sum of all path interactions, each path interaction can be analysed separately and summed together at the end to yield the complete solution. Hence, only one of these individual interactions is considered here. Substitution of Eq. (3.5) into Eq. (3.4) (i.e., cross-correlation between two arbitrary paths), yields, for the integral term:

$$I = \frac{\Gamma^{b_A+b_B}}{(4\pi)^2} \int \frac{e^{ik(L_A-L_B)}}{L_A L_B} \, dz, \tag{3.7}$$

where b_ψ is the number of bottom bounces for the path to receiver ψ, where $\psi = A$ or B, and $L_\psi = \sqrt{x_\psi^2 + (2b_\psi D \pm z \pm z_\psi)^2}$ is the length of the given path between the source, S, and receiver, ψ. The sign in front of z is positive when the wave departing the source is up-going and negative when it is down-going. Similarly, the sign in front of z_ψ is positive when the wave arriving at the receiver is down-coming and negative when it is up-coming.

3.1.1 Stationary phase evaluation

Consider the integrand of Eq. (3.7). Since $1/(L_A L_B)$ varies slowly and the phase $k(L_A - L_B)$ varies quickly within the region of interest, rapid oscillations of the numerator $e^{ik(L_A-L_B)}$ over the integrand allow for the integral, Eq. (3.7), to be solved via the method of stationary phase [68]. Similar interferometric integrals have been solved by others [13, 15, 30]. Here the idea of Snieder *et al.* [30] is followed, but a vertical rather than horizontal line of sources is assumed, and also the theory is extended to a waveguide.

Consider the phase term $k(L_A - L_B)$. The length dependent component, $L_A - L_B$, is the only part that fluctuates over the line integral. The stationary points of the integrand are therefore found by evaluating the partial z derivative of the length dependent part of the phase term, and setting this equal to zero. The source location dependent phase term is

$$
\begin{aligned}
L &= L_A - L_B \\
&= \sqrt{x_A^2 + (2b_A D + \alpha_A z \pm z_A)^2} \\
&\quad - \sqrt{x_B^2 + (2b_B D + \alpha_B z \pm z_B)^2},
\end{aligned}
\tag{3.8}
$$

where $\alpha_\psi = 1$ denotes an up-going wave, and $\alpha_\psi = -1$ denotes a down-going wave, as measured from the source. The partial differential of Eq. (3.8) with respect to z is

$$
\frac{\partial L}{\partial z} = \alpha_A \left(\frac{2b_A D + \alpha_A z \pm z_A}{L_A} \right) - \alpha_B \left(\frac{2b_B D + \alpha_B z \pm z_B}{L_B} \right).
\tag{3.9}
$$

Writing Eq. (3.9) in terms of the acute angle between the path and the vertical, ϕ_ψ , at the point of departure from the source (see Figure 3.1), yields

$$
\frac{\partial L}{\partial z} = \alpha_A \cos \phi_A - \alpha_B \cos \phi_B.
\tag{3.10}
$$

Setting the partial z-derivative to zero yields $\phi_A = \phi_B$ when $\alpha_A = \alpha_B$ (i.e., both waves depart as either up-going or down-going), and $\phi_A = \pi - \phi_B$ when $\alpha_A = -\alpha_B$ (i.e., one wave departs as up-going and the other as down-going). Since both ϕ_A and ϕ_B are less than $\pi/2$, the latter equation has no solutions. Thus a stationary point, defined as a point with geometry satisfying $\frac{\partial L}{\partial z} = 0$, will only occur when both signals depart the source at the same angle. Therefore, the path to the further receiver passes through the closer receiver, as shown in Figure 3.2 for four different paths. Remember that the above derivation holds for any single set of path combinations (i.e., it is true for the direct paths to A and B, for the bottom reflected path to B and the bottom-surface-bottom reflected path to A, and for any other two path combinations), but that the cross-correlation includes the sum of all these path combinations. Not all path combinations will exhibit a

stationary point; for example, the direct path (i.e., no reflections) to A and any boundary interacting path to B will never satisfy $\phi_A = \phi_B$ since ϕ_B will always be less than ϕ_A.
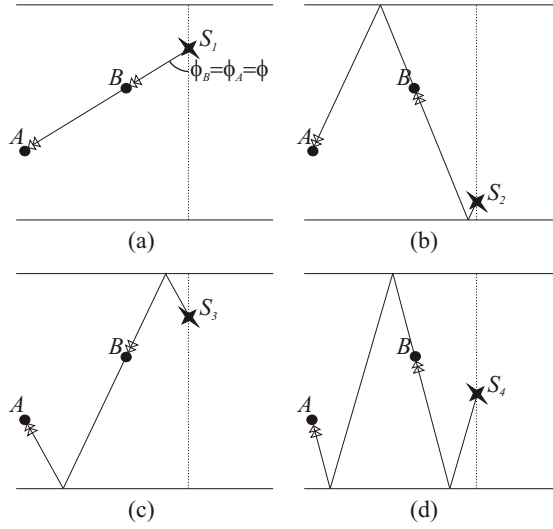

Figure 3.2: Examples of wave paths that correspond to stationary points satisfying $\phi_A = \phi_B = \phi$: (a) direct wave, (b) surface reflected wave, (c) bottom reflected wave, and (d) surface and bottom reflected wave, between the receivers.

The cross-correlation integral, I, Eq. (3.7), can be rewritten within the region of a given stationary point, z_s, as

$$I(z_s) \approx \frac{\Gamma^{b_A+b_B}}{(4\pi)^2} \frac{1}{L_A(z_s)L_B(z_s)} \int_{-\infty}^{\infty} e^{ik(L_A(z)-L_B(z))} \, dz. \tag{3.11}$$

Realistically, the sources exist over the finite limit $(0, D)$; however, extension of these limits to infinity is valid as virtual sources exist over an infinite limit. The phase term can be approximated as a truncated Taylor series within the neighbourhood of any stationary point:

$$L(z) \approx L(z_s) + \frac{(z-z_s)^2}{2} \left(\frac{\partial^2 L}{\partial z^2} \bigg|_{z=z_s} \right), \tag{3.12}$$

with

$$\frac{\partial^2 L}{\partial z^2} \bigg|_{z=z_s} = \sin^2 \phi_s \left(\frac{1}{L_A(z_s)} - \frac{1}{L_B(z_s)} \right), \tag{3.13}$$

41

where $\phi_s = \phi_A = \phi_B$ is the acute (relative to the vertical) departure angle from the source at the stationary point, z_s. Since Eq. (3.12) is evaluated in the region of a stationary point, which is defined as a location where $\frac{\partial L}{\partial z} = 0$, the first order term in the Taylor expansion is also equal to zero. Substituting the phase term and its second derivative, at the stationary point, into the truncated Taylor series, Eq. (3.12), and rewriting the integral, Eq. (3.11), assuming that $L_A(z_s) > L_B(z_s)$ (which is valid since the source is closer to B than to A), yields

$$
\begin{aligned}
I(z_s) = &\frac{\Gamma^{b_A+b_B}}{(4\pi)^2} \frac{e^{ik(L_A(z_s)-L_B(z_s))}}{L_A(z_s)L_B(z_s)} \\
&\times \int_{-\infty}^{\infty} \exp\left(-ik\frac{(z-z_s)^2}{2}\xi\sin^2\phi_s\right) d(z-z_s),
\end{aligned}
\tag{3.14}
$$

where $\xi = \frac{L_A - L_B}{L_A L_B} = \frac{1}{L_B(z_s)} - \frac{1}{L_A(z_s)}$ is the ratio of the difference in path lengths to their product. The term outside the integral takes into account the path lengths and reflection coefficients for the stationary point, and the term inside the integral accounts for the propagation variation in depth relative to the stationary point depth. Equation (3.14) is a Fresnel integral and can therefore be solved by making the substitution $k\frac{(z-z_s)^2}{2}\xi\sin^2\phi_s = \frac{\pi}{2}\tau^2$:

$$
\begin{aligned}
I(z_s) = &\frac{\Gamma^{b_A+b_B}}{(4\pi)^2} \frac{e^{ik(L_A(z_s)-L_B(z_s))}}{L_A(z_s)L_B(z_s)} \\
&\times 2\sqrt{\frac{\pi}{k\xi\sin^2\phi_s}} \int_0^{\infty} \exp\left(-i\frac{\pi}{2}\tau^2\right) d\tau \\
= &e^{i(3\pi/4)}\frac{\Gamma^{b_A+b_B}}{\sin\phi_s}\sqrt{\frac{\xi}{8k\pi}} G_f\left(R(z_s)\right),
\end{aligned}
\tag{3.15}
$$

where $R(z_s) = L_A(z_s) - L_B(z_s)$ is the path length between A and B. Inclusion of the source factor, $n|\rho_s S(\omega)|^2$, from Eq. (3.4), and the relationship

$k = \omega/c$, yields for the cross-correlation between signals at A and B:

$$
\begin{aligned}
C_{AB}(\omega) &= \sum_{z_s} n |\rho_s S(\omega)|^2 I(z_s) \\
&= e^{i(3\pi/4)} n |S(\omega)|^2 \\
&\quad \times \sum_{z_s} \left(\frac{\Gamma^{b_A+b_B} \rho_s^2 G_f\left(R\left(z_s\right)\right)}{\sin \phi_s} \sqrt{\frac{\xi c}{8\pi\omega}} \right),
\end{aligned}
\tag{3.16}
$$

where the summation is over all stationary points.

The relationship in Eq. (3.16) between the cross-correlation of the signals received from a vertical column of sources located in the same vertical plane as two receivers, $C_{AB}(\omega)$ (LHS), and the Green's function, G_f (RHS), is seemingly complicated. The cross-correlation yields an estimation of an amplitude and phase shaded Green's function (i.e., a Green's function that is multiplied by amplitude and phase dependent weighting coefficients). The phase shading is simply a $3\pi/4$ phase shift. If the summed cross-correlations are multiplied by $e^{-i(3\pi/4)}$, phase information, and hence travel times, of the amplitude shaded Green's function can be determined.

The amplitude shading consists of numerous components:

- constant - inverse source spacing term n, medium density term ρ_s^2, sound speed term $\sqrt{c}$, and a $1/\sqrt{8\pi}$ factor;

- path dependent - phase term $\Gamma^{b_A+b_B}$, source departure angle term $\sin \phi_s$, and path length term $\xi = \frac{1}{L_B(z_s)} - \frac{1}{L_A(z_s)}$; and

- frequency dependent - source spectrum term $|S(\omega)|^2$ and frequency factor $1/\sqrt{\omega}$.

Correcting for the constant components is straightforward if the source geometry and medium density and sound speed are known. The frequency dependent terms can be corrected for only if the source spectrum is known. It will, however, be difficult to obtain the correct amplitudes for the path dependent terms since these will be different at each stationary point.

43

The cross-correlation equation, Eq. (3.16), is in this particular form due to the mismatch between a 3D Green's function and a 1D source distribution, as commented by Snieder *et al.* [30]. If a 2D plane instead of the 1D column of sources were used, Eq. (3.4) would be a double integral spanning both the z and y directions, which could be solved as a product of two stationary phase integrals. If either a 2D plane of sources or the far-field approximation of the 2D Green's function, $G(R) = e^{ikr}/\sqrt{r}$, were incorporated, there would not be a dimensionality mismatch, and the sum of the cross-correlations from all sources, Eq. (3.16), would be

$$
\begin{aligned}
\tilde{C}_{AB}(\omega) = &-in|S(\omega)|^2 \\
&\times \sum_{z_s} \left(\frac{\Gamma^{b_A+b_B} \rho_s^2 G_f\left(R\left(z_s\right)\right)}{\sin \phi_s} \times \frac{c}{2\omega} \right),
\end{aligned}
\tag{3.17}
$$

where n is the number of sources per unit surface area for the plane of sources or the number of sources per unit length for the column of sources. Note that there is now no term, apart from the Green's function, containing $L_A(z_s)$ and $L_B(z_s)$, and therefore the amplitude shading is only dependent on the travel path through the $\Gamma^{b_A+b_B}$ and $\sin \phi_s$ terms.

Because of the i/ω factor in Eq. (3.17), the time domain Green's function is proportional to the time-derivative of the summed cross-correlations [11, 13, 15]. Due to a mismatch between the source dimensions and the Green's function, the frequency factor is only $1/\sqrt{\omega}$ in Eq. (3.16). Combining the phase and frequency terms gives $e^{-i(3\pi/4)}/\sqrt{\omega} = i/\sqrt{-i\omega}$. This factor can be corrected for with a $\pi/2$ phase shift, and a 0.5 order fractional time derivative [30, 69]. Note that the $e^{-i(3\pi/4)}$ phase multiplication mentioned earlier is incorporated here.

3.1.2   Incorporation of sediment layers

When the water column is bounded by fully reflective boundaries, as assumed for the preceding derivation, all of the energy is contained within the water column and truncation of the cross-correlation integral in Eq. (3.4) is

avoided. The addition of sediment layers can cause truncation errors since the true integral will then extend to infinity, or at least to the basement (the continental or oceanic crust below the sedimentary layers), to account for sound that interacts with the sediment:

$$C_{AB}(\omega) = |\rho_s S(\omega)|^2 n \int_0^\infty G(\mathbf{r}_A, \mathbf{r}_S) G^*(\mathbf{r}_B, \mathbf{r}_S)\, dz. \qquad (3.18)$$

If the source column is restricted to the water, the calculated integral still ceases at D and the stacked cross-correlations yield a poorer estimation of the frequency and phase shaded Green's function. Consider as an example a purely theoretical reflective environment, with constant sound speed, consisting of a water column and M sediment layers. The length of any path between the source, S, and receiver, ψ, becomes

$$L_\psi = \sqrt{x_\psi^2 + \left(2pD + \sum_{m=1}^M (2q_m D_{sm}) \pm z \pm z_\psi\right)^2}, \qquad (3.19)$$

where p and q_m are the multiple order (the number of reflections off the bottom of the layer plus the number of refractions into the layer from below) in the water and each sediment layer, m, and D_{sm} is the depth of the mth sediment layer. The stationary phase condition is still $\phi_A = \phi_B$; however, there exist paths satisfying this condition whose path length differences are not identical to any of the Green's function path lengths, direct or otherwise, between the two receivers. For example, in Figure 3.3(a) the path to receiver B is a reflection from the sediment-water interface. The path to receiver A is a transmission through this interface, a reflection from the basement and a transmission back into the water. The stationary phase condition of $\phi_A = \phi_B$ is satisfied; however, the path length difference is

$$\begin{aligned} L = &\sqrt{x_A^2 + (2D + 2D_s - z - z_A)^2} \\ &- \sqrt{x_B^2 + (2D - z - z_B)^2}, \end{aligned} \qquad (3.20)$$

which, in general, differs from the path length of any wave that travels between the two receivers, and therefore should not contribute to the Green's

function. The arrival due to this stationary point is therefore called a 'spurious' arrival. Note that the path length difference and hence the time at which spurious arrivals occur is dependent on the horizontal distance separating the source column from the receivers. If the column of sources, S, were extended into the sediment (sources in the sediment are denoted S'), a second stationary point would exist, as shown in Figure 3.3(b), cancelling the contribution of the water-source stationary point.
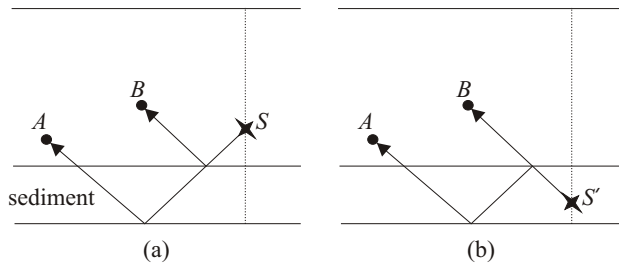

Figure 3.3: Example of (a) water source, S, and (b) sediment source, S', stationary points that have the same path length to each receiver, and therefore the same path length difference. They are opposite in phase and therefore cancel with one another and do not contribute to the Green's function.

In order for the equal amplitude criterion to be met, when sources span an area of varying impedance the amplitude of the cross-correlations should be normalised by division with $\frac{\rho_s c}{\sin \theta_s}$. In practice this normalisation factor can be difficult to incorporate since the angle of departure from the source is variable. If, however, only changes in density are considered, then the normalisation is simplified and the cross-correlations need only be divided by the density at the source location before summing.

More complex paths may exhibit multiple stationary points, located in both the water column and the sediment, corresponding to a particular path length difference; however, they will sum to zero so long as the source column spans all paths that have a stationary point.

Truncations in the integral of Eq. (3.18) may also be apparent as peaks in the summed cross-correlation at time intervals corresponding to cross-

correlations between paths from sources located at the water-sediment interface. Consider, as an example, the paths depicted in Figure 3.4(a)-(c). As sources closer to the water-sediment interface are considered, the direct paths, shown as solid lines in Figure 3.4(a), converge to the direct paths from a source in the sediment, shown as dashed lines in Figure 3.4(a). At the bottom of the sediment these paths converge with the bottom bounce paths, shown as solid lines in Figure 3.4(b), which in turn converge to the dashed paths shown in Figure 3.4(c) at the water-sediment interface.

Sediment sources would, of course, be difficult to incorporate experimentally. The theory here is therefore important for understanding how the more realistic configuration in which the sources are limited to the water column will affect the summed (over all sources) cross-correlation. If the sources in the sediment are not included in the summation, discontinuities in the integral will exist at the water-sediment interface for the water source paths in Figure 3.4(a) and (c). The path length difference for this
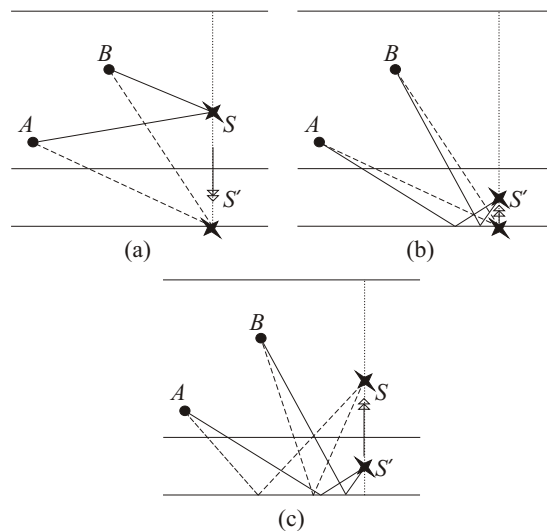

Figure 3.4: The direct paths, solid lines in (a), and bottom bounce paths, dashed lines in (c), are linked via a continuous transition through sediment source configurations (b); a truncation of the integral results in a discontinuity in the arrival structure of the paths if sediment sources are not considered.

discontinuity is

$$\Delta L = \sqrt{(D - z_A)^2 + x_A^2} - \sqrt{(D - z_B)^2 + x_B^2}$$
$$- \left(\sqrt{(D - z_A + 2D_s)^2 + x_A^2} - \sqrt{(D - z_B + 2D_s)^2 + x_B^2} \right), \tag{3.21}$$

where D_s is the depth of the sediment. If the sediment is shallow ($D_s \ll D$), these discontinuities may not be observable in the summed cross-correlations since the path length differences for a source at the sediment-water interface will be small; however, if the sediment is deep, the discontinuity may be observed as two distinct spurious peaks separated temporally by $\Delta L/c$.

Restricting the sources to the water column can therefore lead to spurious peaks in the cross-correlation function. If the sources are extended through the sediment and the cross-correlation function is normalised by the density at the source, these spurious peaks may be avoided.

3.1.3 Spurious arrivals

Snieder *et al.* [30] and Sabra *et al.* [15] determined that spurious arrivals also exist for their particular geometries and environments. The spurious arrivals that they discuss and the ones described here are all due to the volume of interest not being fully enclosed by sources (i.e., acoustic paths exist between the volume of interest and the external environment that are not sampled, or intersected, by the source line or plane). Each of these aberrations are, however, distinct.

The spurious arrivals described in Section 3.1.2 occur when the sources are limited to the water column. The integral does not extend to infinity resulting in two causes of spurious arrivals. As the source approaches the upper and lower boundaries, the surface and the basement, different paths will converge. Hence, when the sources are contained within the water column, paths which would converge at the sediment bottom do not converge, creating a gap in the cross-correlation integral. Spurious peaks therefore occur at these path discontinuities. The second mechanism of spurious ar-

rivals is a stationary-phase contribution from a source in the water column that does not actually contribute to the full Green's function, such as described in Section 3.1.2 in conjunction with Eq. (3.20). This contribution occurs from cross-correlations between waves that are reflected at the water-sediment interface and waves that pass into the sediment. It should cancel with a stationary-phase contribution of equal amplitude and opposite phase from the sediment. For example, the contribution from the cross-correlation of the paths in Figure 3.3(a) cancels with that from Figure 3.3(b). When these sediment sources are not included a false peak will be recorded.

Sabra *et al.* [15] modelled time-averaged surface generated ambient noise using a horizontal plane of point sources at a constant depth in a waveguide. The spurious arrivals they described are caused by stationary-phase contributions from cross-correlations between a wave that initially undergoes a surface reflection and one that does not. For an isovelocity water column one wave departs at an angle of ϕ from the horizontal, and the other departs at an angle of $-\phi$. These stationary points are intrinsic to the horizontal source configuration. If the depth of the plane of sources is reduced, the spurious peaks converge to the same time delay as the true Green's function paths; however, they are π out of phase and will still result in shading of the Green's function.

Snieder *et al.* [30] used a horizontal line of evenly spaced sources in a homogeneous medium, with one or more horizontal reflectors below and no free surface above. The assumption of there being no free surface means that the spurious paths described by Sabra *et al.* did not exist in Snieder's analysis. The spurious arrivals described by Snieder *et al.* are due to false stationary-phase contributions caused by cross-correlation of waves reflected from distinct reflectors, which occur due to the sources only being in the upper layer. To eliminate these spurious multiples, a second surface of sources would have to be included below the bottom reflector.

3.1.4 Variations in sound speed profile

Introduction of a varying sound speed profile will further complicate the problem. A conceptual argument describing the effect of a sloped sound speed profile specific to the source geometry under consideration is presented here.

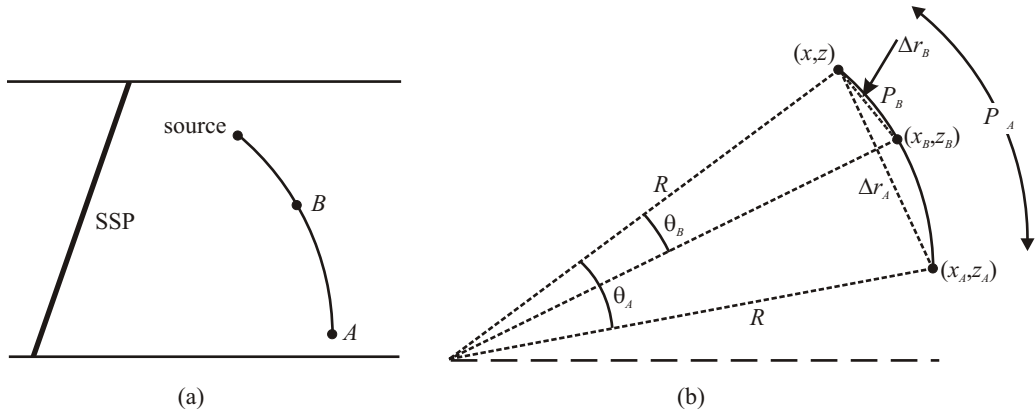Consider the geometry of Figure 3.5. The downward refracting sound

Figure 3.5: (a) Waveguide with a downward refracting sound speed profile. (b) Geometry associated with the curved ray paths, P_A and P_B, from the source to the receivers A and B respectively.

speed profile results in curvature of the ray path towards the region of lower sound speed. The linear distance that sound travels from source to receiver ψ is

$$\Delta r_\psi = \sqrt{(x_\psi - x)^2 + (z_\psi - z)^2}. \tag{3.22}$$

Also, using the cosine rule:

$$\Delta r_\psi^2 = 2R^2 - 2R^2 \cos \theta_\psi. \tag{3.23}$$

Equating Eq. (3.22) and Eq. (3.23), and rearranging to express in terms of θ_ψ yields

$$\theta_\psi = cos^{-1} \left(1 - \frac{(x_\psi - x)^2 + (z_\psi - z)^2}{2R^2} \right). \tag{3.24}$$

The length dependent component of the phase term of Eq. (3.7) becomes

$$L = P_A - P_B = R(\theta_A - \theta_B). \tag{3.25}$$

Differentiating Eq. (3.25) with respect to z and simplifying yields

$$\frac{\partial L}{\partial z} = \frac{z - z_A}{\sin \theta_A} + \frac{z_B - z}{\sin \theta_B}. \tag{3.26}$$

The partial z-derivative is equal to zero when

$$\frac{z - z_A}{\sin \theta_A} = \frac{z - z_B}{\sin \theta_B}. \tag{3.27}$$

The curvature of the ray path in Figure 3.5(b) has been exaggerated so that the geometry can be more clearly seen. Small changes in sound speed profile will refract the ray path only slightly and hence the radius R becomes large and angles θ_A and θ_B become very small. Using this small angle approximation, equality of Eq. (3.27) is achieved when the origins of arcs P_A and P_B coincide. The stationary phase condition is therefore still achieved when the ray path to receiver A passes through receiver B.

Using a ray-geometric approximation, Snieder *et al.* (Appendix A of [30]) present work that generalises their arguments for the direct wave in a homogeneous medium to a direct wave in a heterogeneous medium with variations in velocity that are sufficiently smooth for ray theory to remain applicable. The environment and geometry used here are different to that of Snieder *et al.*; however, the idea of generalising from a homogeneous to a heterogeneous medium is the same.

3.1.5 Generalised environment

The environments considered in the previous sections all have simplifying assumptions. It needs to be confirmed that the theory does, indeed, carry over to more realistic environments. An understanding of differences that may present themselves, and also of potential limitations that a more realistic environment may present, is therefore important.

In a realistic environment, attenuation as well as the aforementioned variations in sound speed profile and the effect of sediment layers needs to be considered. The inclusion of attenuation adds complications since it will generally result in the paths not cancelling exactly; the degree to which they will cancel one another is environment dependent.

In a generalised environment, the mathematics becomes more complex; however, the fundamental ideas hold. An amplitude and phase shaded Green's function will still be obtained by summing the density normalised source cross-correlations, so long as the source column spans the water column and all underlying sediments. The effect of limiting the sources to the water column, upon the similarity between the summed cross-correlations and the shaded Green's function, is environment dependent.

3.1.6 Simulations

Three simulation environments were selected to clearly demonstrate application of OAI from a physical perspective. The Green's function between two receivers is approximated using the OAI approach for a vertical line of sources. OASES [49] was used for both the OAI approach and to compute the true Green's function between the receivers. The theory derived via the method of stationary phase in previous sections is used only for discussion purposes.

The environments, depicted in Figure 3.6, comprise (a) an isovelocity waveguide with a purely reflective bottom; (b) a completely reflective environment with an isovelocity waveguide and an isovelocity sediment layer; and (c) a more realistic environment with a downward refractive sound speed profile (SSP) waveguide, and an upward refractive SSP sediment layer. Receivers A and B are located at depths of $80\,\mathrm{m}$ and $50\,\mathrm{m}$, respectively. The two receivers are separated $100\,\mathrm{m}$ horizontally. A column of sources, spaced at $0.5\,\mathrm{m}$ increments, spans the water column in the same vertical plane as the two receivers, $40\,\mathrm{m}$ to the right of receiver B. The source is a Ricker wavelet with a centre frequency of $350\,\mathrm{Hz}$.
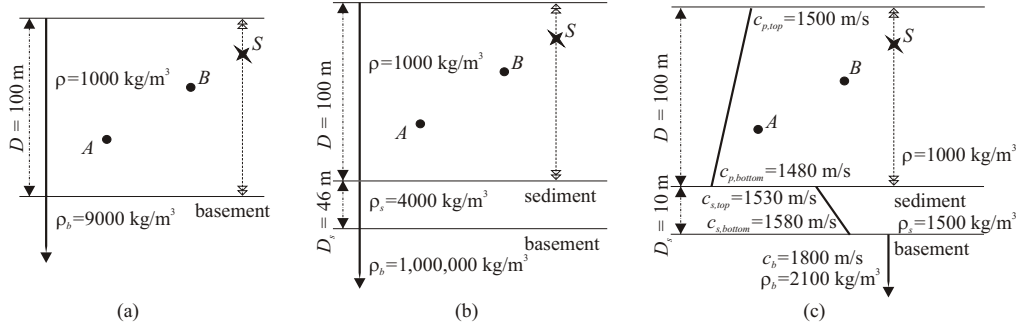
Figure 3.6: Simulated waveguide environments: (a) isovelocity waveguide with a purely reflective bottom (constant $c = 1500\,\mathrm{m/s}$); (b) isovelocity purely reflective waveguide with a sediment layer (constant $c = 1500\,\mathrm{m/s}$); and (c) more realistic refractive environment with a sediment layer. A large basement density is used in (a) to increase the amplitudes of bottom-reflected paths, and an unrealistically large value is used in the basement of (b) to give unity reflection at the bottom of the sediment.

The sum of the cross-correlations, Eq. (3.4), is evaluated by treating the integral as a sum over the source column. For each source location the acoustic pressure at A and B is evaluated assuming a constant source spectrum of $S(\omega)$. The pressures are cross-correlated, normalised by the density at the source, and then summed over the source locations and compared to the frequency and phase shaded Green's function between the two receivers:

$$\frac{\rho\,|S(\omega)^2|}{\omega}e^{i(3\pi/4)}G(R). \tag{3.28}$$

The unstacked cross-correlations, which are the cross-correlations from sources at each depth plotted as a function of source depth, are shown in Figure 3.7 for each simulation environment. Peaks in the cross-correlation functions are visible at times corresponding to differences between the travel time of an acoustic path from the source to receiver A, and the travel time of an acoustic path from the source to receiver B. The path length differences increase or decrease, depending upon the particular paths in question, for sources lower down the water column. The corresponding correlation peak therefore occurs at a later or earlier time. The changes in correlation peak times are visible as curves in the unstacked correlations in Figure 3.7. The

curves converge with several others at the top and bottom of the acoustic environment because different paths converge to the same length at these extremities. For example, a direct path and a surface-reflection path will converge at the waveguide surface.

Isovelocity waveguide

Both the unstacked cross-correlations and the stacked response, which is the sum of the cross-correlations over all source depths, $\sum C$, are depicted in Figure 3.7(a) for the isovelocity waveguide. The peaks in the stacked response, $\sum C$, occur due to the Fresnel zones in the vicinity of each stationary point. The $3\pi/4$ phase and $|S(\omega)|^2$ amplitude shaded simulated Green's function, G, is also included for comparative purposes. The peaks in the Green's function, G, occur at the travel times of each acoustic path between receivers A and B, and it is these peaks that the cross-correlations are attempting to replicate.

The direct path stationary point is the temporal maximum of the direct wave cross-correlation arrival structure to each receiver. It occurs at $38\,\mathrm{m}$ depth at a time of $0.070\,\mathrm{s}$. The direct path time difference converges to $0.065\,\mathrm{s}$ for sources towards the surface, and to $0.052\,\mathrm{s}$ for sources towards the bottom. These endpoints do not, however, result in spurious peaks in the stacked response, because they converge with other paths for sources at the given boundary. Stationary points corresponding to arrivals of the reflected paths are more difficult to see as they occur at locations very close to the waveguide boundaries; however, they can still be seen in the stacked response. For example, the peak in the stacked cross-correlations at $0.109\,\mathrm{s}$, circled in red, corresponds to the stationary point of the bottom bounce path to receiver B and the bottom-surface bounce path to receiver A, which occurs at a depth of $98\,\mathrm{m}$ and is therefore difficult to distinguish.

Overall, the phase of the stacked cross-correlation shows good agreement with the frequency and phase shaded Green's function, with only minor deviations. The amplitude is not accurate, but this can be explained by
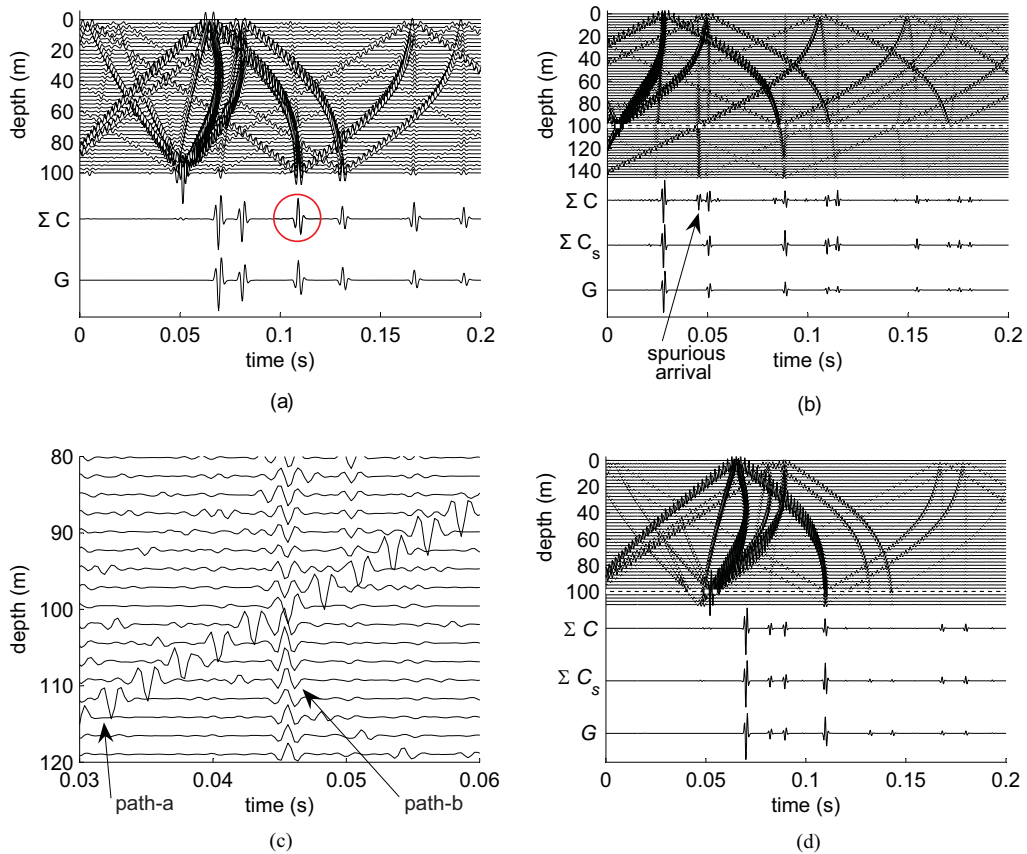
Figure 3.7: The cross-correlations for (a) the isovelocity waveguide, (b) the reflective environment with a sediment, (c) a magnified portion of (b), and (d) the refractive environment, are plotted as a function of depth. The water-sediment interfaces in (b) and (d) are marked by a dashed white line. The stacked cross-correlation from a column of sources in the water, $\sum C$, the stacked trace with sediment sources included for (b) and (d) only, $\sum C_s$, and the shaded Green's function, G, are also plotted. The two paths indicated in (c) are the arrivals for the ray paths depicted in Figure 3.8.

the difference in amplitude between the stacked cross-correlations and the Green's function due to path dependent components, $\Gamma^{b_A+b_B}$, ϕ_s and ξ, as derived in Eq. (3.16).

Waveguide with single sediment layer

This particular waveguide environment was chosen in order to see the effect of a sediment layer upon the stacked cross-correlation. In order to emphasise what is happening the receivers are separated only 30 m horizontally, the Ricker wavelet centre frequency has been doubled to 700 Hz, and the source column spacing halved to 0.25 m. The remainder of the source/receiver configuration is identical to that of the isovelocity waveguide example.

Both the unstacked cross-correlations and the stacked responses are shown in Figure 3.7(b). The stacked response for the case when the source column terminates at the water-sediment interface, $\sum C$, contains the arrival paths observable in the shaded Green's function, G; however, it also contains several spurious arrivals, the most noticeable of which occurs within the time interval 0.044-0.047 s. The stacked response with sediment sources included, $\sum C_s$, is plotted for comparison. Such a configuration would likely not be implemented in practice, but is useful here for explaining the results from the line water column sources. The stacked response with sediment sources does not contain the spurious arrivals. The spurious arrivals observable in $\sum C$ are due to the source column not continuing through the sediment and therefore not producing a perfect time-reversal mirror.

One contribution to this spurious arrival is due to the discontinuities in the arrival structure caused by truncation of the $C_{AB}(\omega)$ integral at the bottom of the water column. The two paths affected are shown in Figure 3.8(a) and (b) and their cross-correlations, depicted in Figure 3.7(c), are denoted path-a and path-b respectively. Path-a and path-b are cross-correlation peaks corresponding to differences in arrival times between paths from the source to each receiver, and as such, should not be confused with the individual acoustic paths. For sources near the water-sediment interface the
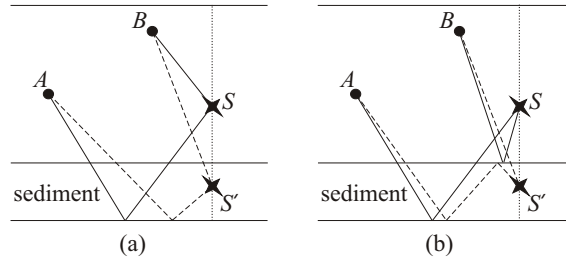
Figure 3.8: Two possible sets of ray paths: (a) direct path to B and the bottom bounce path to A; and (b) a path to B with one water-sediment bounce and a path to A that has two transmissions through the interface. In both cases the solid lines represent paths from sources in the water, denoted S, and the dashed lines represent paths from sources in the sediment, denoted S'.

arrival time for path-a, the solid line in Figure 3.8(a), transitions smoothly with the solid line, path-b, of Figure 3.8(b). This can be seen by examining the arrival structure in Figure 3.7(c). The two arrivals do not, however, cancel each other. For both path-a and path-b the path length difference between the source and each receiver decreases for sources closer to the sediment, as shown in Figure 3.7(c) and Figure 3.9. The two sets of ray paths are also in phase, as shown in Figure 3.7(c). The two arrivals will therefore sum together to contribute to the largest spurious arrival in trace $\sum C$ of Figure 3.7(b).

If the sources are extended through the sediment to the basement then the summation over the arrival structure corresponding to Figure 3.8 cancels completely at the water-sediment interface. At the interface the cross-correlation of the solid line representation of path-a, see Figure 3.8(a), will transition smoothly into the dashed line representation of path-a both in terms of arrival time and amplitude. For path $A + B$ the number of transmissions through the sediment remains constant. The difference in path length continues to decrease for sources at greater depths and there is no phase change, see Figure 3.7(c). Cancellation at the interface therefore occurs. Path-b also transitions smoothly; however, this time the difference in path length has a local minimum at the water-sediment interface. The vari-

ation in path length difference is small as a function of depth and hence this is difficult to see in Figure 3.9. The phase of the cross-correlation is inverted at the interface, as shown in Figure 3.7(c), resulting in direct cancellation. For sources closer to the basement, the arrival structure and amplitude will transition smoothly into that of other paths. For example, path-a will converge to the same arrival time as all other combinations of direct and single basement bounce paths to A and B, and since the amplitudes of each set of paths will be the same, a smooth transition between the paths will occur.

A second contribution to the largest spurious arrival is a stationary-phase contribution from a source in the water column which does not actually contribute to the full Green's function, as explained in Section 3.1.2. An example schematic of the scenario is shown in Figure 3.3(a). The solid line of path-b should not contribute to the Green's function as the signal received by A never passes through B, regardless of the source depth; however, a stationary point exists when the two paths depart the source at the same angle (i.e., 67.3 m source depth). This stationary point is difficult to see in the stacked response since the difference in path length of Figure 3.8(b) varies by less than a metre ($\sim \frac{\lambda}{5}$) over the entire depth, see Figure 3.9. As seen in Figure 3.9, a second stationary point exists within the sediment at a depth of 133 m. If the sources are extended through the sediment then this stationary point annuls the contribution from the stationary point in the water column.

As expected, the largest spurious peak from the water source column cross-correlation is not observable in the stacked cross-correlation of the column of sources that extends through the sediment in trace $\sum C_s$ of Figure 3.7(b). Other deviations from the expected shaded Green's function are also reduced or removed.

Refractive environment with sediment

The source and receiver geometry and source type are identical to that of the original isovelocity waveguide example. The stacked responses for the
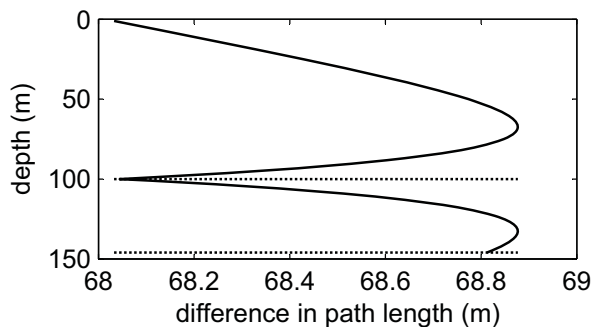
Figure 3.9: The difference between the path lengths from the source to receiver A and the source to receiver B as a function of source depth for the ray path geometry of Figure 3.8(b). The horizontal dotted lines represent the water-sediment interface and the sediment bottom.

water column sources only, $\sum C$, and for the case where the sources extended through sediment, $\sum C_s$, as well as the shaded Green's function, G, are shown in Figure 3.7(d). The phase of the water column stacked response is in reasonable agreement with that of the shaded simulated Green's function. The path time differences have converged almost completely to their sediment-bottom interface value at the water-sediment interface and hence the spurious arrivals which were easily observed in the previous example are not apparent here. Even if the source column could be extended into the sediment, only a minor increase in accuracy would be obtained. These results agree with the simulations of Roux and Fink [29], who concluded that the effect of limiting sources to the water column is negligible when the modal continuum of the sediment is small relative to that of the water.

3.2   Horizontal straight line towed source

Ocean acoustic interferometry can be performed using a horizontal line, rather than a vertical column, of sources. The source is towed along a horizontal line in the end-fire plane of the receivers, starting directly above one receiver, and travelling away from the receivers. The relationship between the summed cross-correlation and the Green's function is derived, using the

methodology of Section 3.1, to be [15, 30]

$$C_{AB}(\omega) = e^{i(3\pi/4)} n |S(\omega)|^2 \sum_{p_s} \left(\frac{\Gamma^{b_A + b_B} \rho_s^2 G_f(R(x_s))}{\cos \phi_s} \sqrt{\frac{\left(\frac{1}{L_B(x_s)} - \frac{1}{L_A(x_s)} \right) c}{8\pi\omega}} \right).$$

(3.29)

3.3 Horizontal hyperbolic towed source

OAI using a straight line tow source relies on the fact that the horizontal distance from the source to receiver A is always $x_A - x_B$ further than to receiver B, where the x axis has been specifically defined as the horizontal axis between A and B. A second tow-source configuration in which the horizontal distance to each receiver differs by a constant amount is described here.

Consider Figure 3.10, which is a geometrical view of the source, p_n, and receivers, A and B, from above. The source location, p_n, which varies as a function of ϕ, the angle from the line connecting A and B, is defined as being a constant distance, Δr, further from receiver A than B (i.e., the distance from B is x_n and the distance from A is $x_n + \Delta r$). If the receiver B is defined as the origin then the location of p_n is

$$p_n = (x_n \cos \phi, \pm x_n \sin \phi).$$

(3.30)

For the case when $\phi = 0$ (i.e., p_n lies upon the horizontal line joining A and B), p_n and x_n are denoted p_0 and x_0 respectively.

Although the horizontal difference in distance from the source p_n to the receivers A and B is a constant value Δr, this distance is $2x_0$ smaller than the horizontal distance between the receivers, and therefore the hyperbolic configuration is set-up to perform OAI not between receivers A and B, but between receiver A and a virtual receiver V located Δr from A. Note that unlike the straight line tow source this configuration assumes that acoustic paths are azimuth independent, that is, the acoustic path of the signal leaving the source point p_n will be the same over the distance x_n in both
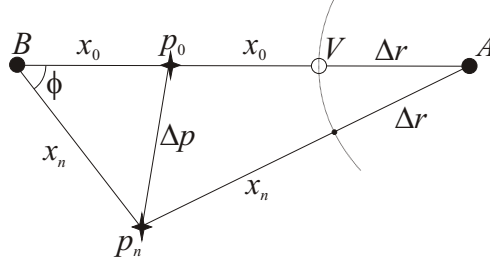
Figure 3.10: Geometrical construct for determining the equation governing the location of point p_n, which is a constant Δr further from A than B.

the direction towards A and the direction towards B, and the acoustic path between A and any point Δr from A will be constant. The technique is therefore only applicable in a range independent environment.

From geometry:

$$(x_n + \Delta r)^2 = x_n^2 + (2x_0 + \Delta r)^2 - 2(x_n)(2x_0 + \Delta r)\cos(\phi). \qquad (3.31)$$

Rearranging to express in terms of ϕ yields

$$\phi = \cos^{-1}\left(\frac{2x_0^2 + 2x_0\Delta r - x_n\Delta r}{x_n(2x_0 + \Delta r)}\right). \qquad (3.32)$$

The points p_n therefore form a hyperbola which has its asymptotic origin at the point midway between the two physical receivers, A and B, its x-intercept at the midpoint of receiver B and the virtual receiver, V, located between the two physical receivers at the same depth as the first receiver, and its focus at receiver B, as shown in Figure 3.11. If the origin of the system is assumed to be at the first receiver B, and the second physical receiver A lies along the positive x-axis, the governing equation can then be written in the form

$$x^2 = -\sqrt{a^2\left(1 + \frac{y^2}{b^2}\right)} - c, \qquad (3.33)$$

where $a = (2x_0 + \Delta r)/2$, $c = a - x_0$ (x_0 is the location where the hyperbola crosses the x-axis), and $b = -\sqrt{c^2 - a^2}$.
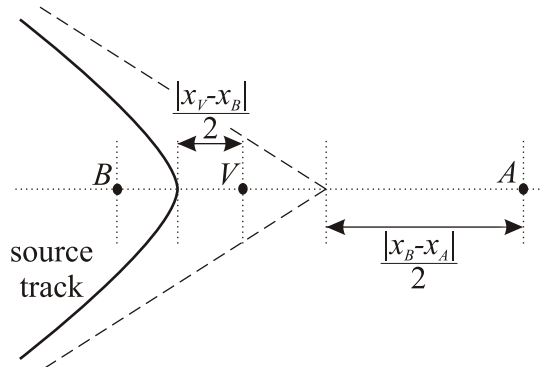
Figure 3.11: Hyperbolic source track as viewed from above. The hyperbola apex passes midway between receiver A and virtual receiver B and the asymptote is midway between B and A.

The hyperbola converges to the straight line scenario as $x_0 \to 0$. Hence the hyperbolic tow-source can be considered to be a similar geometrical set-up to the straight line scenario, although in this case, the horizontal difference in path length is a constant value of $x_A - x_V$. The resulting cross-correlation sum will therefore relate to the Green's function between the virtual receiver, V, and receiver A rather than the Green's function between the two physical receivers, B and A. It must be remembered, however, that unlike the straight line scenario, the hyperbolic configuration relies upon range independence.

3.4 Conclusion

A stationary phase argument was used to theoretically describe the relationship between the summed cross-correlations from a line of active sources, and the Green's function between two hydrophones. The theory and simulations for the vertical line source presented here were shown to be in agreement with a modal approach presented by others, and results for cross-correlations of towed horizontal line and hyperbolic sources were shown to be in agreement with theoretical work on cross-correlations of wave gen-

erated ocean noise, modelled as a horizontal plane of sources, as well as horizontal lines of seismic surface sources. It was demonstrated that in a range independent environment the Green's function can be approximated from cross-correlations of a horizontal hyperbolic towed source with its apex at a location horizontally between two physical hydrophones.

All three OAI source scenarios: the source column, straight line towed source, and hyperbolic towed source, have their advantages and drawbacks. The source column is located in a region close to both receivers and therefore attenuation is minimal, but suffers from there being no sources in the underlying sediment and hence the modal continuum of the sediment is not fully accounted for [29].

The towed source scenarios are advantageous in that once the source is deployed the only consideration is the ship path; however, they suffer from intrinsic stationary-phase contributions from cross-correlations between a wave that initially undergoes a surface reflection and one that does not. If the source depth is reduced, the spurious arrivals converge to the same travel time as the true Green's function paths; however, they are π out of phase and will result in shading of the Green's function. The hyperbolic towed source method is the only non *end-fire* tow-source geometry that is feasible. The source must, in this case, have its apex at a location horizontally between two physical hydrophones. It has the advantages of being able to approximate the Green's function between a physical receiver and a virtual receiver and, since the sources do not have to be near either receiver, of being accessible even when buoys mark the beginning and end of arrays; however, it suffers from the disadvantages that the hyperbola can be difficult for a ship to navigate, and the theory assumes range independence.

Experimental results for cross-correlation of sound from a vertically lowered source and a horizontally towed source will be presented in Chapter 6, and compared with experimental results from cross-correlation of ship dominated ambient noise.

Chapter 4

Experimental Environment

This chapter describes the underwater environment where all of the experimental data presented in this thesis were obtained, as well as the equipment used. The techniques used to process and analyse the data are described in Chapters 5 and 6.

The empirical data used in this thesis were collected during the Shallow Water 2006 (SW06) experiments [70]. This chapter starts with an overview of the SW06 experimental location, measurement equipment, acoustic sources, and ocean sound speed profiles (SSPs). The effects of the local water SSP upon acoustic propagation are then explained. It is shown that due to the steep thermocline of the ocean SSP, the ocean-only signal (no interactions with surface or bottom of water column) is often not from a direct arrival; rather, it is an interference of many propagation paths. This suggests that it is likely to be difficult to extract meaningful information from a reflection coefficient inversion, which is based on comparison of the amplitude of the direct ocean path to that of the bottom reflected path. A reflection coefficient inversion was performed and was found to only obtain a sediment sound speed within a 60 m/s range, though values estimated by others [71, 72] do lie within these bounds, supporting the validity of the results presented here. A relationship between sub-bottom arrival times, where sub-bottom paths are defined as those that penetrate the underlying

sediment, and sediment sound speed is also estimated using a time-domain analysis, but the limited angular coverage of the bottom interacting acoustic paths prevents the decoupling of sediment thickness and sound speed.

4.1 Overview of experiment

The SW06 experiment was a large scale collaborative shallow water acoustic experiment, combining both low frequency ($<$ 1000 Hz) and medium frequency (1000–10,000 Hz) acoustic tests, conducted off the Eastern US seaboard, at the location shown in Figure 4.1(a). Dozens of research bodies, seven ships, 62 moorings, and aircraft and satellite coverage, were all used in the experiments that ran from mid-July to mid-September 2006 [70]. Data pertinent to this thesis were collected on four hydrophone arrays between August 30 and September 6 using the deployment vessel R/V *Knorr*.

The four hydrophone arrays that were used for acoustic data collection are:

- MPL-VLA1 (*Marine Physical Laboratory - Vertical Line Array 1*), a 16 element array operated by Scripps Institution of Oceanography;

- SWAMI32 (32 hydrophone *Shallow Water Acoustic Measurement Instrumentation*), an L-shaped array operated by ARL-UT (Applied Research Laboratories, The University of Texas at Austin);

- SWAMI52, a 52 hydrophone L-shaped array also operated by ARL-UT; and

- Shark, a 48 element L-shaped array operated by Woods Hole Oceanographic Institute [75].

The locations of these four hydrophone arrays are shown in Figure 4.1(b). Detailed descriptions of the arrays are included in Appendix B. Photographs of the MPL-VLA1, SWAMI32 and Shark instrumentation are included in Figure 4.2.
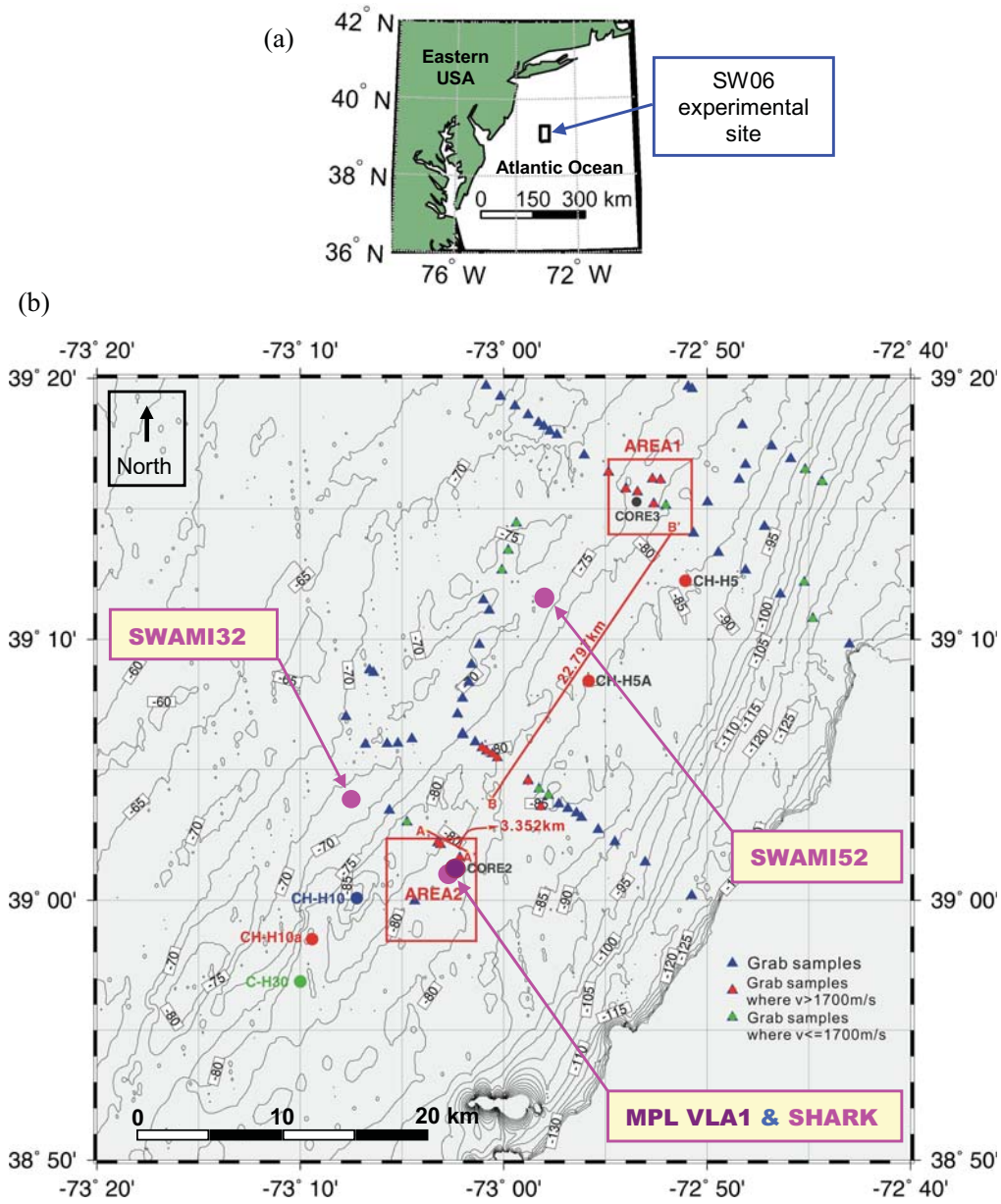
Figure 4.1: (a) Geographic location of the SW06 experimental site on the New Jersey Shelf. (b) Locations of the four hydrophone arrays. Triangles mark locations for which sediment grab sample data (information about the sediment determined from the collection and analysis of small physical samples) exists [73]. The contours represent water depth in metres. (b) is adapted from [74].

(a) (b)

(c) (d)
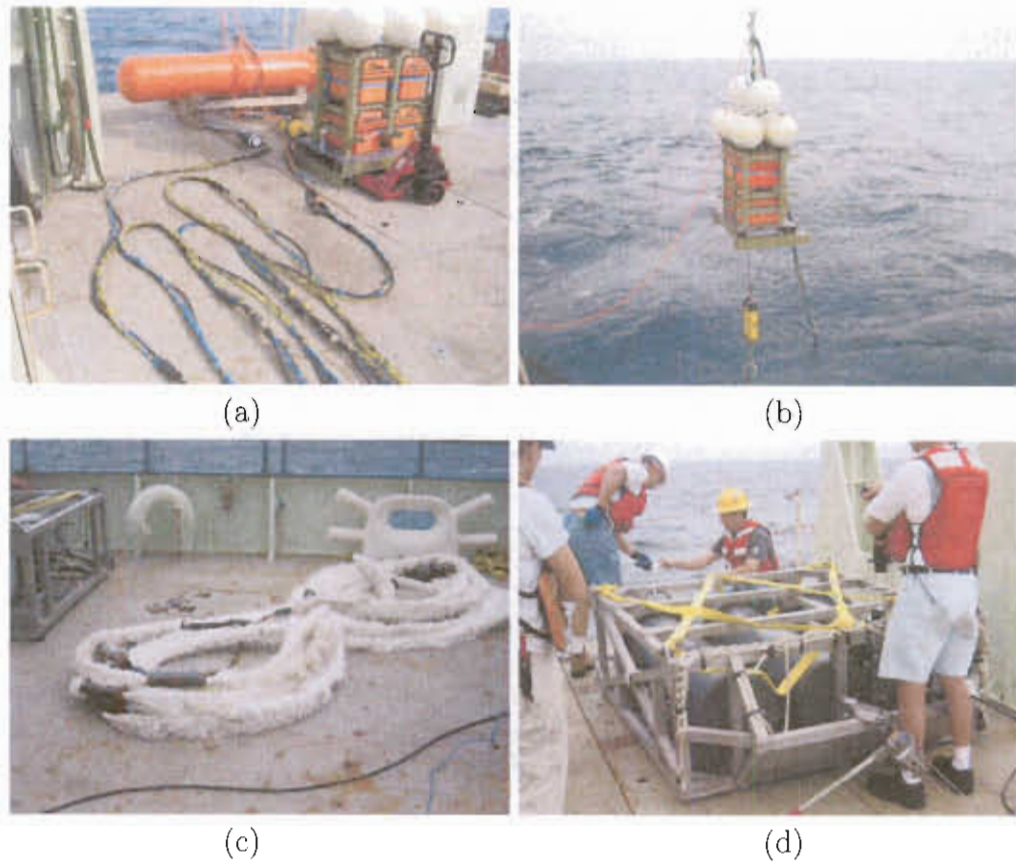
NOTE: This figure is included on page 68 in the print copy of the thesis held in the University of Adelaide Library.

(e)

Figure 4.2: Hydrophone array equipment prior to deployment. (a) MPL-VLA1: 16 element hydrophone array (front); electronics module with pressure case and flotation mounted on a fiberglass box structure (right); and torpedo-shaped buoyancy float (back). (b) MPL-VLA1 electronics module being lowered into the ocean. The yellow package just above the water is a dual acoustic release tilt/heading/depth sensor. (c) SWAMI32 vertical line array. (d) SWAMI32 electronics module. (e) Shark electronics battery sled with part of the HLA/VLA coiled on top. (e) is sourced from [75].

Acoustic signals were recorded from several different source types. All of the controlled source signals were emitted by a mid-frequency free flooded ring transducer source (model ITC-2015), as shown in Figure 4.3(a). The source depth was controlled by a ship-board winch, as shown in Figure 4.3(b). The sound sources used were:

- a 1500–4500 Hz linear frequency modulated (LFM) pulse (Section 4.2.2);

- ambient noise (Chapter 5);

- R/V *Knorr* ship noise (Chapter 6);

- a 1100–2900 Hz LFM pulse (Chapter 6 and Section 7.2.2); and

- a broadband 1100–2950 Hz energy pulse (Section 7.2.2).

(a)   (b)

Figure 4.3: Photographs of (a) the ITC-2015 mid-frequency source, and (b) the source being controlled using a ship-board winch (Note the cable ties that were used to control the joystick position, and hence rate of descent, when the source needed to be lowered at a slow but constant rate!).

4.1.1 Sound speed profiles

Water column properties were recorded using Sea-bird 911*plus* CTD (conductivity, temperature, depth) instrumentation [76]. The profiler records

oxygen content, fluorescence, light transmission, density, salinity and temperature as a function of depth, and the SSP is interpolated from this data. Two CTD profiles were taken during each recording, one as the CTD device was lowered to just above the seafloor, and one as it was raised to the surface. The up-going profile was ignored as the CTD sensors are on the bottom of the device and therefore the device itself would have interfered with measurements on the up-going track. Twenty five CTDs were measured from the R/V *Knorr* platform between August 30 and September 6, and the SSPs from these are shown in Figure 4.4. Tropical Storm Ernesto passed through the experimental region on September 2, creating high sea states and strong wind conditions. The SSPs recorded after the storm exhibit a deeper mixing layer, which was forced by the increase in wave energy during the storm. The sound speed of the mixing layer is also lower due to the incorporation of the lower temperature waters from below the original mixing layer.

4.2   Analysis of experimental environment

Data from a mid frequency (1500–4500 Hz) LFM source were recorded on August 31. The data were recorded on MPL-VLA1, which was arranged as shown in Figure 4.5(a). The array was deployed in a water depth of 79 m. The first element (hydrophone 1) was 8.2 m above the seafloor, and inter-element spacing was 3.75 m. Using dynamic positioning, the source was held at a constant range 230 m from the array, and slowly lowered down the water column, being held at water depths of 15–65 m in 10 m increments for 5 min at each source depth. Clipping of the recorded signal was observed periodically in the upper 30 m of the water channel. All clipped data were discarded.

CTDs 36 and 37 were recorded at the beginning and end of the source lowering. The SSP from each of these CTDs is shown in Figure 4.5(b).
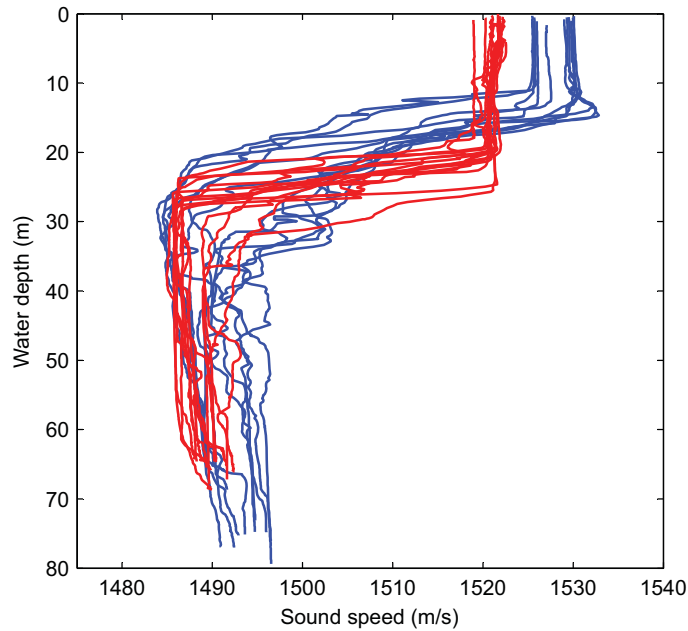
Figure 4.4: SSPs recorded from all CTDs measured from R/V *Knorr* between August 30 and September 6. Blue line profiles were recorded before Tropical Storm Ernesto and red line profiles were recorded after the storm.
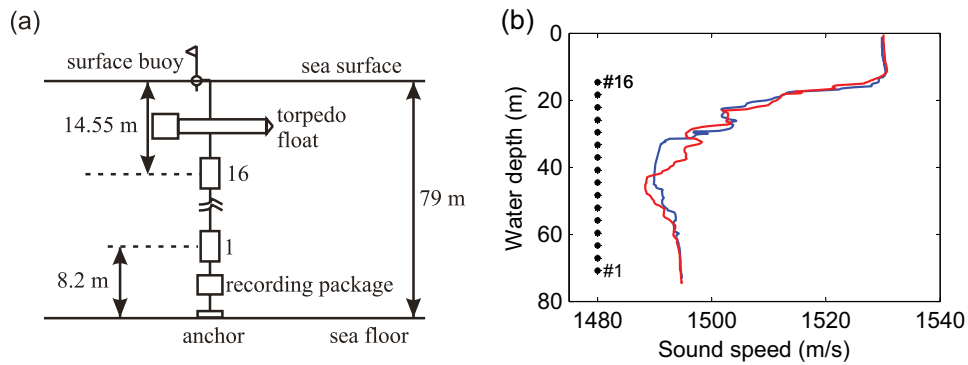

Figure 4.5: MPL-VLA1 array (a) geometry, and (b) SSPs from CTDs 36 (blue) and 37 (red). The 16 black markers in (b) represent the hydrophone depths.

4.2.1 Effects of ocean sound speed profile

The two SSPs of Figure 4.5(b) show similar characteristics: an almost isovelocity layer extending down to less than 20 m depth below the ocean surface, followed by a steep thermocline over which the sound speed drops about 40 m/s within 20 m, and then a more gentle sound speed increase towards the bottom. SSPs with similar characteristics have been recorded at nearby locations by Badiey *et al.* [77], who showed that small changes in sound speed within the thermocline have large effects upon acoustic transmission.

In an isovelocity waveguide the ocean-only paths are straight lines, and hence the amplitude of the received signal is virtually uniform over the waveguide depth. If a varying SSP exists, the sound may be refracted such that at some locations multiple ocean-only paths intersect, whilst at others there is no ocean-only path at all. The effect of sound speed variations on the ocean-only paths for the experimental environment was modelled using OASES (*Ocean Acoustics and Seismic Exploration Synthesis*) wavenumber integration based software [49], first using the SSP of CTD36 (SSP36), and then using the SSP of CTD37 (SSP37). Sources within or below the thermocline are refracted in such a way as to create interference patterns; however, these patterns are highly sensitive to the SSP. Consider, for example, the ocean-only path fields created by a source depth of 45 m shown in Figure 4.6(a)–(b). Interference patterns can clearly be seen for both SSPs, but their locations are distinct. For example, the results assuming SSP36, depicted in Figure 4.6(a), show a high amplitude around hydrophones 15 and 11–12, but if SSP37 is assumed, the amplitude is low, as shown in Figure 4.6(b). Similarly, the high amplitude seen between hydrophones 7 and 8 assuming SSP37, does not exist for SSP36.

The source at 15 m depth is around the top of the thermocline and this causes a large shadow zone at and below the thermocline, as shown in Figure 4.6(c). The signal, which is shown in Figure 4.6(d) for both sound speeds, is less sensitive to SSP changes although there are some regions where significant differences are observable, such as above 15 m and

from 35–55 m. For the other source depths large SSP dependent amplitude variations occur over short variations in depth, as is shown in Figure 4.6(e)–(g). These variations in the direct path amplitude mean that comparing the direct and bottom bounce path amplitudes for reflection coefficient inversion is difficult.
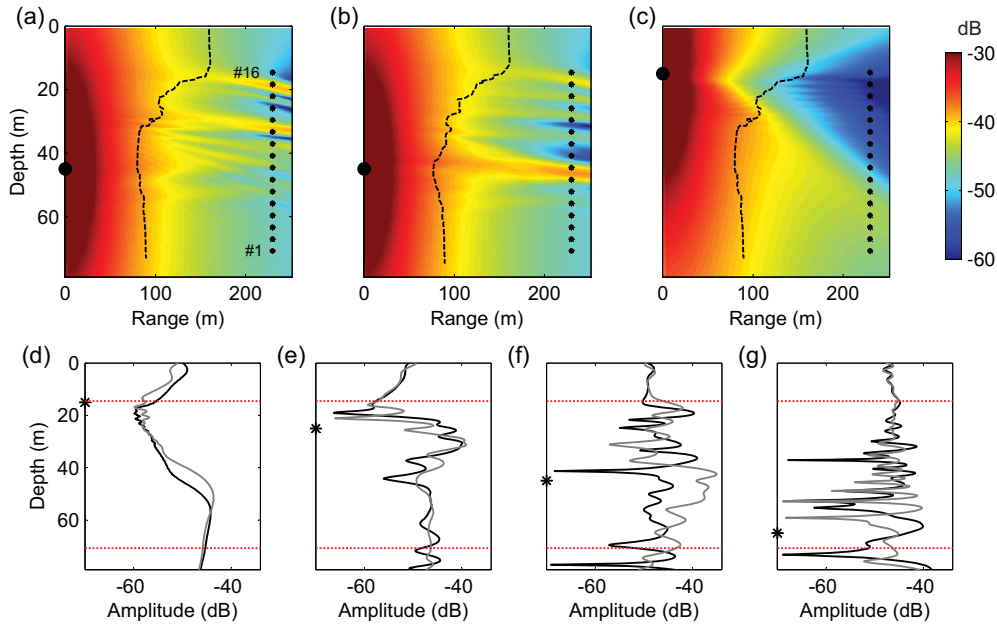

Figure 4.6: Modelled pressure amplitude (dB relative to source amplitude) of the 2200 Hz ocean-only field versus range and depth for source depths of (a) 45 m (SSP36), (b) 45 m (SSP37), and (c) 15 m (SSP36). The shape of the SSP as a function of depth is overlaid as a black dashed line (see Figure 4.5(b) for exact values). The large black circles mark the source location, and the 16 black markers at 230 m range represent the VLA locations. Plots (d)–(g) show the amplitude versus depth at 230 m range using SSP36 (black) and SSP37 (grey) for source depths of (d) 15, (e) 25, (f) 45, and (g) 65 m (black asterisks). The horizontal dotted lines represent the top and bottom of the VLA.

4.2.2   Reflection coefficient inversion

Reflection coefficient inversion has been successfully performed by others and the methodologies are well understood [78]. It is applied here to mid-

frequency data collected on August 31. Signals received for a source depth of 15 m were considered since they have the largest grazing angles, and will therefore have the most paths above the critical angle of reflection. The signals were matched filtered with a 1 second 1500–4500 Hz LFM pulse replica signal. The matched filter correlates the signal with the energy and amplitude normalised replica by multiplication in the frequency domain. A Hilbert transform is then applied; negative frequency components are set to zero and positive frequency components below the Nyquist frequency are doubled. The envelope of the inverse Fourier transform is then calculated. For each hydrophone depth, 300 chirps were measured. The envelope of the match filter outputs for each chirp are shown in Figure 4.7(a).

Results of Bellhop [48] finite-element ray tracing in the water column, using the measured SSPs, showed that the surface and bottom reflected paths are less sensitive to changes in SSP than direct paths. For bottom and surface bounce paths over a 230-m range, the ray paths are nearly straight lines. Thus the reflection coefficient can be extracted by comparing the amplitudes of these paths. The amplitude ratio of the bottom and surface reflected signals was compared to that of an OASES model assuming perfect reflections; however, sensible values for reflection coefficients could not be obtained. This is likely due to the inherent difficulty in generating an accurate model of the ocean surface for reflection problems [4]. The bottom reflected to direct path ratios of the experimental and simulated data were therefore compared instead.

The SSP was assumed to be that of CTD36 since the 15-m source depth signals were recorded at a time close to this measurement. The data from hydrophones in the central part of the array were discarded since signals in this region are most sensitive to SSP variations, as can be seen in Figure 4.6(d). Inclusion of these data would likely have yielded results that were highly erroneous if the actual and assumed SSPs differed. For the bottom four hydrophones (1–4), a reflection coefficient of unity was estimated, suggesting that the received signal is below the critical angle. For the top
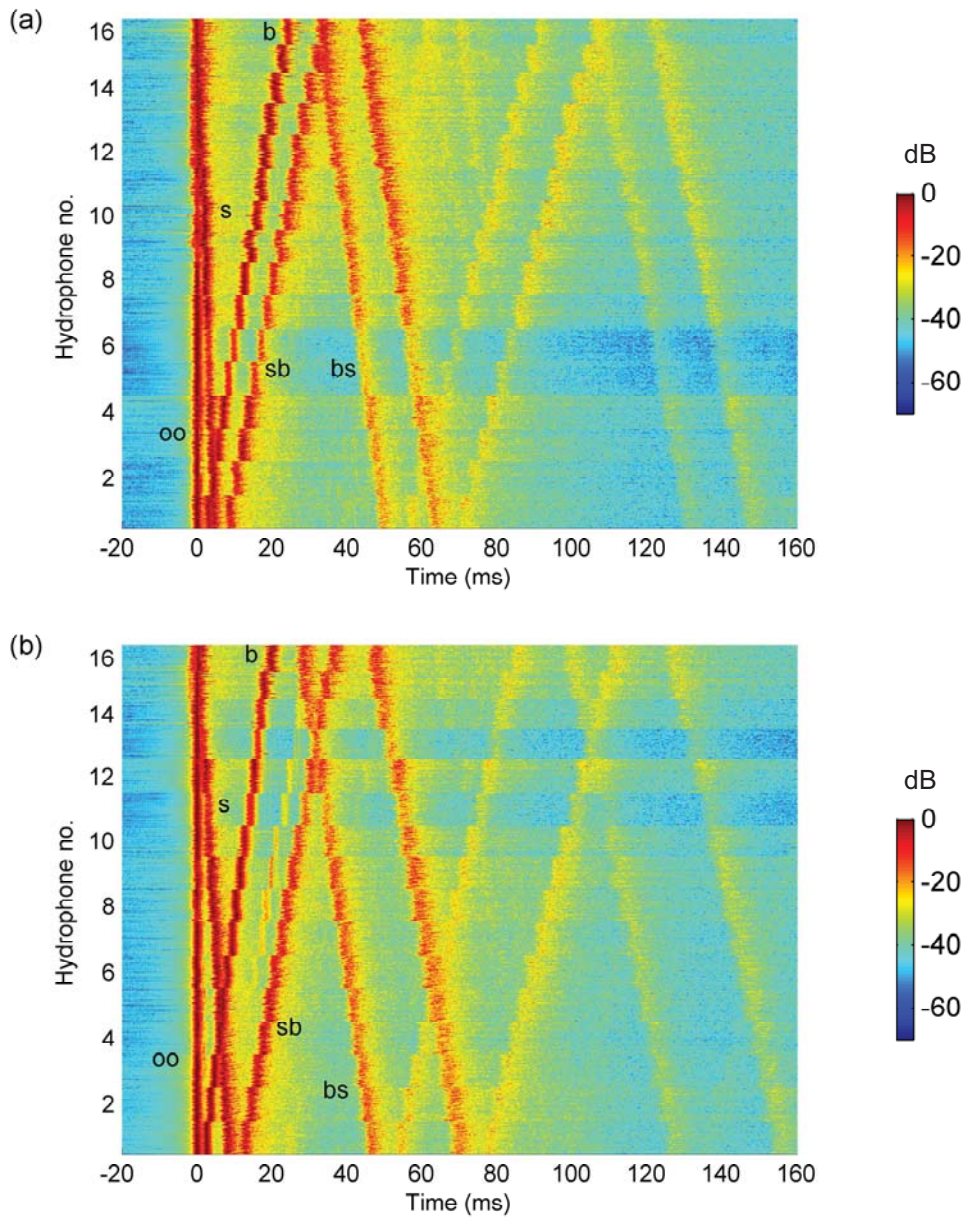
Figure 4.7: Match filter of 1500–4500 Hz chirp, recorded on all 16 hydrophones for a source depth of (a) 15m, and (b) 25m. For each hydrophone depth, 300 chirps were measured and the match filter from each of these is displayed here in a stacked arrangement at that depth. The amplitude (dB) is relative to the highest amplitude of the match filter for each chirp. The arrival paths are denoted oo (ocean-only), s (surface bounce), b (bottom bounce), sb (surface-bottom bounce) and bs (bottom-surface bounce), and time is relative to the ocean-only arrival.
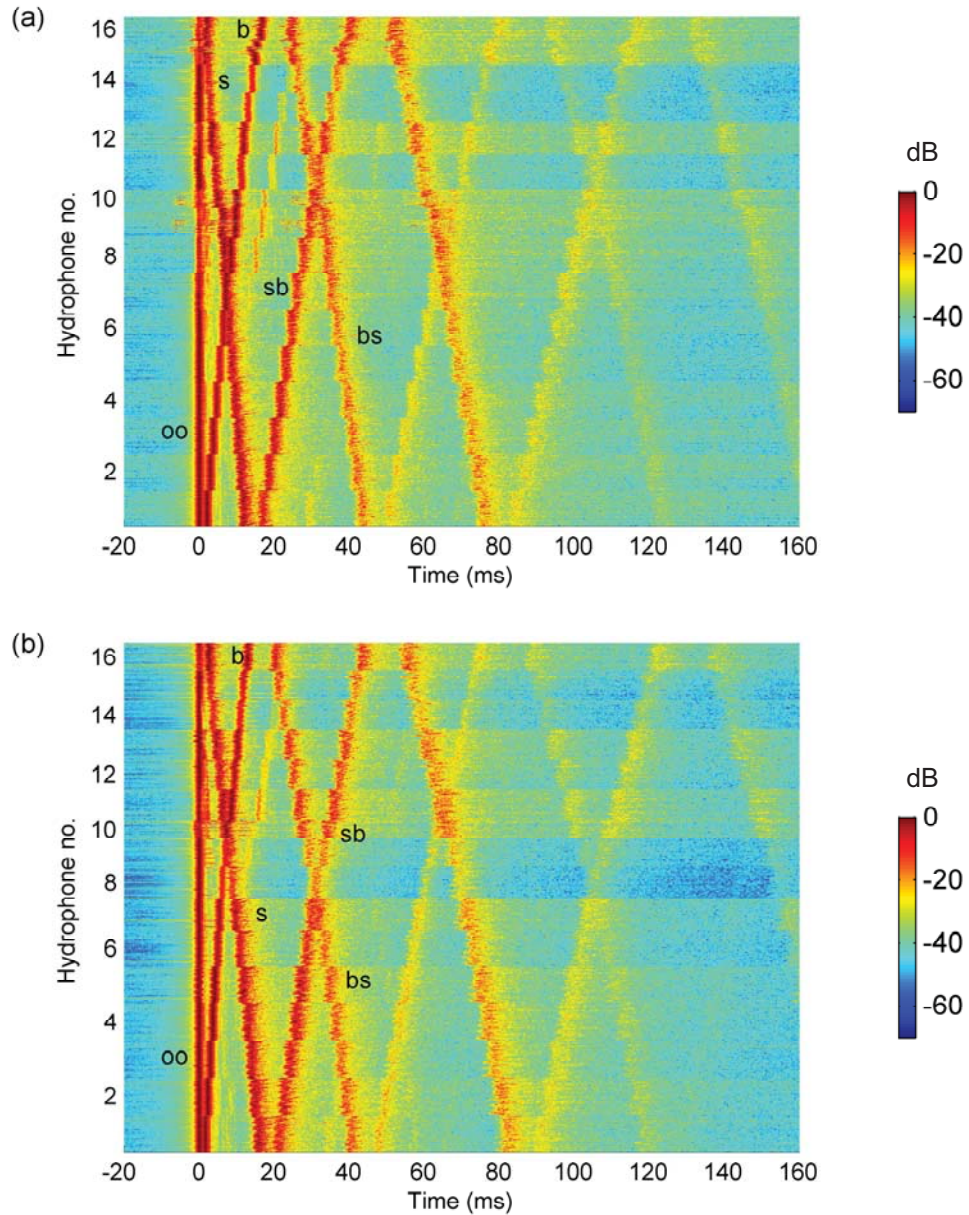
Figure 4.8: Match filter of 1500–4500 Hz chirp, recorded on all 16 hydrophones for a source depth of (a) 35m, and (b) 45m. For each hydrophone depth, 300 chirps were measured and the match filter from each of these is displayed here in a stacked arrangement at that depth. The amplitude (dB) is relative to the highest amplitude of the match filter for each chirp. The arrival paths are denoted oo (ocean-only), s (surface bounce), b (bottom bounce), sb (surface-bottom bounce) and bs (bottom-surface bounce), and time is relative to the ocean-only arrival.

four hydrophones (13–16) a reflection coefficient of 0.4 was estimated. This suggests a critical angle of 20–25°, corresponding to a sediment sound speed of 1590–1650 m/s, which is in agreement with Jiang and Chapman [71] and Huang *et al.* [72].

4.2.3   Sub-bottom arrival time inversion

The envelopes of the matched filtered signals for each chirp for source depths of 25, 35 and 45 m are plotted in Figure 4.7(b) and Figure 4.8. Definite sub-bottom arrivals can be seen as peaks in the amplitude between the third and fourth major arrivals (i.e., between the bottom and surface-bottom paths) for 15 source-hydrophone pairs: 25-m source depth, hydrophones 7–12; 35-m source depth, hydrophones 8–13; and 45-m source depth, hydrophones 11–13. Sub-bottom arrivals were expected for the 15-m source depth; however, these occurred around the time of the surface-bottom reflected paths, and hence cannot be individually discerned.

The arrival time difference between the bottom and sub-bottom paths was calculated for each of the 15 source-hydrophone pairs. Time differences ranged from 1.32 ms (35 m source depth, 45.15 m hydrophone depth) through 1.88 ms (35 m source depth, 25.4 m hydrophone depth). These arrival time differences relate to the sediment sound speed and thickness. The square of the observed difference and modelled difference assuming a specific sediment depth and sound speed was determined for each source-hydrophone geometry. The sum over all source-hydrophone pairs:

$$\sum([t_{\mathrm{sb}} - t_{\mathrm{b}}]_{\mathrm{obs}} - [t_{\mathrm{sb}} - t_{\mathrm{b}}]_{\mathrm{mod}})^2, \tag{4.1}$$

is plotted versus sediment thickness and sound speed in Figure 4.9, and exhibits a line of minima (line of deepest blue extending from 0 m sediment thickness at 1500 m/s sediment sound speed, through 33 m sediment thickness at 1900 m/s sediment sound speed) showing the optimal combination of sediment sound speed and layer thickness. Ideally a minimum point corresponding to a single sound speed and sediment thickness would have been

obtained, but the parameters are coupled here because the time difference is related to the layer thickness divided by sound speed. A larger angular coverage of the different geometries would create a better determined minimum.

Although a definite minimum could not be obtained, bounds on the sediment thickness can still be obtained for the sound speeds estimated in Section 4.2.2. Based on Figure 4.9, if a sound speed of 1590–1650 m/s is assumed, a sediment thickness of 5–11 m is estimated, which is significantly lower than the thickness values of just over 20 m predicted by others [71, 72, 79]. However, Jiang and Chapman [71] suggest a negative gradient sound speed in the sediment, and this could give a slightly larger inverted sediment thickness. Ideally the sub-bottom arrival inversion would search over sediment thickness, sediment sound speed at the top, and sound speed slope within the sediment, but insufficient data are available to successfully search over multiple variables.
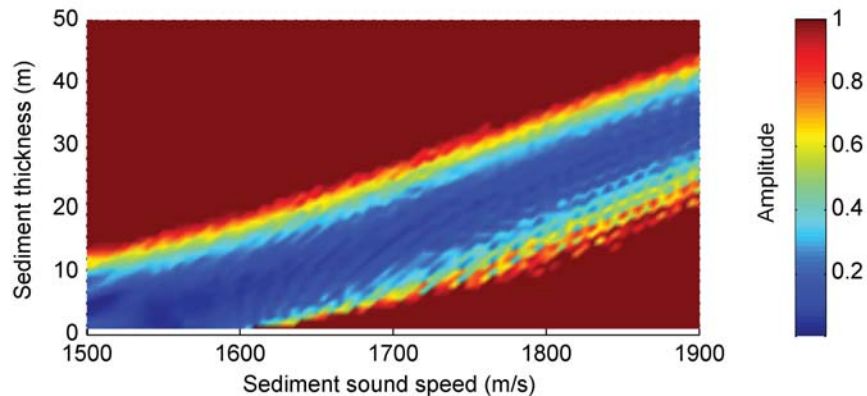

Figure 4.9: The square of the difference between the measured bottom and sub-bottom time differences, and the modelled values, is summed over all source-hydrophone geometries, and the result is threshold clipped to 3.2% of the maximum so that low amplitude structure can be better observed. The amplitude is normalised to the threshold value.

4.2.4   Conclusion

The ocean environment of the SW06 experiment was characterised by a strong thermocline and significant spatiotemporal variability. The resulting direct path acoustic field is shown to consist of multi-path interference, with high sensitivity to ocean variations. It is therefore difficult to extract accurate reflection coefficient information from the acoustic data. Attempts to do so provided, at best, approximate values.

An inversion based on time differences between bottom reflected and sub-bottom arrival times estimated the relationship between sediment sound speed and sediment thickness; however limited angular coverage of the ray paths prevented decoupling of these variables.

Simulated data will be used to compare with and support experimental results in Chapters 5 and 6. If the inversion results obtained here had been more conclusive, they could have been used to specify sediment properties for the simulation input environments, but given that they are not, it was decided that sediment properties would be better estimated from nearby sediment grab sample data [73]. All simulated data in the upcoming chapters will therefore use sediment property estimates based upon grab sample data.